Old Dominion University Research Foundation

A DIAMOND ELECTRON TUNNELING MICRO-ELECTROMECHANICAL SENSOR

Final Report
Project: NAG-1-1995

Submitted By

Dr. Sacharia Albin
Principal Investigator
Microelectronics Research Laboratory
Department of Electrical & Computer Engineering
Old Dominion University
Norfolk, Virginia 23529, USA

May 12, 2000

A DIAMOND ELECTRON TUNNELING MICRO-ELECTROMECHANICAL SENSOR

Final Report
Project: NAG-1-1995

Submitted By

Dr. Sacharia Albin
Principal Investigator
Microelectronics Research Laboratory
Department of Electrical & Computer Engineering
Old Dominion University
Norfolk, Virginia 23529, USA

May 12, 2000

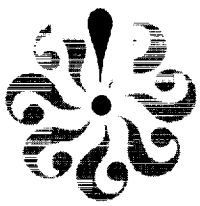

SUMMARY

A new pressure sensing device using field emission from diamond coated silicon tips has been developed. A high electric field applied between a nano-tip array and a diaphragm configured as electrodes produces electron emission governed by the Fowler - Nordheim equation. The electron emission is very sensitive to the separation between the diaphragm and the tips, which is fixed at an initial spacing and bonded such that a cavity is created between them. Pressure applied to the diaphragm decreases the spacing between the electrodes, thereby increasing the number of electrons emitted.

Silicon has been used as a substrate on which arrays of diamond coated sharp tips have been fabricated for electron emission. Also, a diaphragm has been made using wet orientation dependent etching. These two structures were bonded together using epoxy and tested. Current - voltage measurements were made at varying pressures for 1 - 5 V biasing conditions. The sensitivity was found to be 2.13 mV/V/psi for a 20 x 20 array, which is comparable to that of silicon piezoresistive transducers.

Thinner diaphragms as well as alternative methods of bonding are expected to improve the electrical characteristics of the device. This transducer will find applications in many engineering fields for pressure measurement.

TABLE OF CONTENTS

PAGE
LIST OF TABLES iv

LIST OF FIGURES v

I. INTRODUCTION 1

II. THEORY OF FIELD EMISSION BASED SENSOR 20
2.1 Electron Emission 20
2.2 Silicon Diaphragm 37
2.3 Theoretical Analysis 42
2.4 Diamond as an Emitter 44

III. EXPERIMENTS 46
3.1 Processing Steps 46
3.1.1 Cleaning 46
3.1.2 Oxidation 47
3.1.3 Lithography 52
3.1.4 Orientation Dependent Etching 54
3.2 Device Fabrication 60
3.2.1 Nano-tip Array 60
3.2.2 Diaphragm 67
3.2.3 Diamond Growth 70
3.2.4 Bonding 73
3.3 Testing 73

IV. RESULTS AND DISCUSSION 76
4.1 Field Emitter Array and Diaphragm 76
4.3 Pressure Transducer Characteristics 79
4.4 Discussion 84

V. CONCLUSIONS 89
5.1 Future Research 89
5.1.1 Temperature Dependence 89
5.1.2 Sensitivity 90
5.1.3 Bonding 90
5.2 Applications 91

REFERENCES 94

LIST OF TABLES

TABLE PAGE

1. Ranges of absolute pressure gauges 4

2. Properties of diamond 45

3. Rate constants for wet oxidation of silicon 50

4. Transducer Sensitivity 88

LIST OF FIGURES

FIGURE PAGE

1. U-tube manometer 5
2. McLeod pressure gauge 6
3. Wallace-Tiernan mechanical diaphragm pressure gauge 8
4. Cross-section through a capacitance manometer 9
5. Sketch of Knudsen-type pressure gauge 11
6. Pressure sensing elements..... 13
7. Typical structure of silicon capacitive pressure sensor 15
8. Cross-section of silicon diaphragm with piezoresistors 16
9. Silicon pressure sensor using and FEA..... 19
10. PE diagram..... 22
11. Electron tunneling through the potential barrier..... 25
12. Tunneling transmission coefficient 27
13. Electron emission through potential barrier for a semiconductor..... 34
14. Field emission through potential barrier with field penetration into the interior of the semiconductor..... 36
15. Current density versus diaphragm separation from the FEA..... 38
16. Diaphragm deflection versus pressure for various thicknesses..... 41
17. Current density as a function of the diaphragm spacing from the FEA..... 43
18. Schematic of horizontal oxidation furnace and bubbling system..... 49
19. Wet thermal oxide thickness versus oxidation time..... 51
20. Lithography process and the effect of positive resist..... 53

21. Cubic cell of diamond lattice with (100) plane 56

22. Cubic cell of diamond lattice with (110) plane 57

23. Cubic cell of diamond lattice with (111) plane 59

24. Etching feature with respect to mask opening of (100) plane 61

25. Orientation dependent etching of (100) plane through patterned SiO_2 mask 62

26. Mask used to create nano-tip array 63

27. Schematic representation of nano-tip array fabrication process 65

28. Etching sequence of nano-tip array 66

29. Typical silicon nano-tip array 68

30. Silicon nano-tip at high magnification 69

31. Cross-section of typical diaphragm 71

32. Microwave Plasma Chemical Vapor Deposition (MPCVD) System 72

33. Typical diamond-coated array 74

34. Test setup used for pressure sensor 75

35. Diamond coated FEA 77

36. Diamond coated nano-tip 78

37. Voltage vs. Pressure Graph for Applied Voltage of 1 Volt 81

38. Voltage vs. Pressure Graph for Applied Voltage of 5 Volts 82

39. Voltage vs. Pressure Graph at constant temperature 83

40. Semi-log plot of Voltage vs. Pressure for applied voltage of 1 Volt 85

41. Voltage vs. Pressure Graph for Applied Voltage of 5 Volts 86

42. Nano-tip array and diaphragm on same substrate 93

I. INTRODUCTION

Pressure is a fundamental design parameter. Since the first mercury barometer was conceived by Evangelista Torricelli more than 300 years ago, numerous devices and techniques have been designed and implemented for the accomplishment of pressure measurement.

The following equations form the basis for devices fabricated to measure pressure [1]. In mechanics, pressure is the force per unit area

$$p \equiv \frac{dF}{dA} . \tag{1}$$

In hydraulics, pressure is specific weight times height

$$dp \equiv -wdh \tag{2}$$

where the negative sign accounts for the change in height of the fluid that is being compressed. In kinetics, pressure is molecular kinetic energy per unit volume

$$p \equiv \frac{2}{3}\frac{KE}{V} = NRT \tag{3}$$

In thermodynamics, pressure is the work per unit volume

$$p \equiv \frac{dW}{dV} . \tag{4}$$

The symbols in equations 1-4 are defined as follows:

A area

F force

h	height
KE	kinetic energy
N	number of molecules per unit volume
p	absolute pressure
R	specific gas constant
T	absolute temperature
V	volume
w	specific weight
W	work

Pressure is measured on many different scales, and although the standard that has been adopted is the Pascal (N/m^2), other scales are frequently used. These include pounds per square inch (psi), inches of water (in. H_2O), inches of mercury (in. Hg), atmospheres (atm), bars, millibars (mbar), microbars (μbar), millimeters of mercury (mm Hg) or Torr, dyn/cm^2, kg/cm^2, kg/m^2, and microns (μ). Each scale can be converted to any other scale with an appropriate conversion factor, which can be found in most physics text books [2], the CRC Handbook of Chemistry and Physics [3], and other literature dealing with pressure measurement [1, 4].

The earliest pressure measuring device, used in 1662 by Robert Boyle for the precise determination of steady fluid pressures [1], is the U-tube manometer [1, 5, 6]. This was the first example of an absolute gauge, i.e., a gauge that measures total pressure, but whose calibration depends only on geometric or mechanical factors [7]. Other absolute gauges include the McLeod gauge of 1874 [1, 4 - 10], the Wallace-Tiernan

mechanical diaphragm gauge [1, 8], the capacitance gauge [1, 7], and the Knudsen gauge of 1910 [7 - 10]. Table 1 [7] shows a summary of the performance of each of these gauges. Since these gauges are accepted as standards for pressure measurement, an explanation of each is presented in the following paragraphs.

As shown in Figure 1 [5], the U-tube manometer consists of a liquid filled tube shaped in the form of a U with one leg of the tube subjected to a reference pressure and the other to an unknown pressure. By measuring the difference in height, Δh, and knowing the specific gravity of the liquid and the reference pressure, the unknown pressure is determined according to

$$\Delta p = w_M \Delta h \tag{5}$$

where Δp is the difference between the known pressure and the reference pressure and w_M is the specific weight of the fluid in the tube.

The operation of the McLeod gauge, shown in Figure 2, is relatively simple. All of the mercury is initially contained in the volume below the cutoff level. The gauge is exposed to an unknown gas pressure, p_1; the mercury is then raised in tube A beyond the cutoff, trapping a gas sample of initial volume $v_1 = V + \alpha h_c$, where α = area of the measuring capillary. The mercury is continuously forced upward until it reaches the zero level in the reference capillary B. The mercury in the measuring capillary C reaches a level, h, where the gas sample is at its final volume $v_2 = \alpha h$, and at the final amplified manometric pressure $p_2 = p_1 + h$. The relevant equations at these pressures are

$$p_1 v_1 = p_2 v_2 \tag{6}$$

Table 1: Ranges of absolute pressure gauges [7].

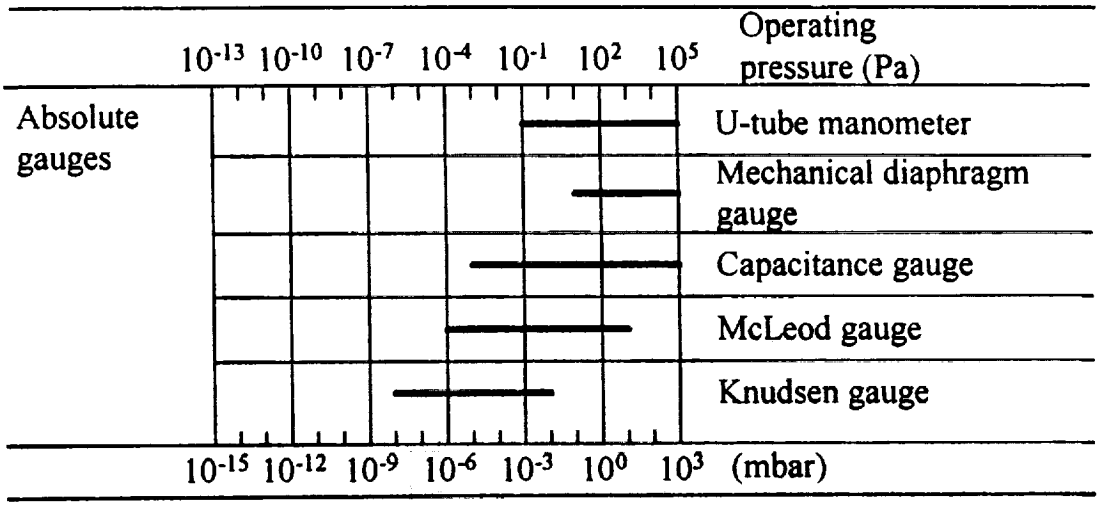

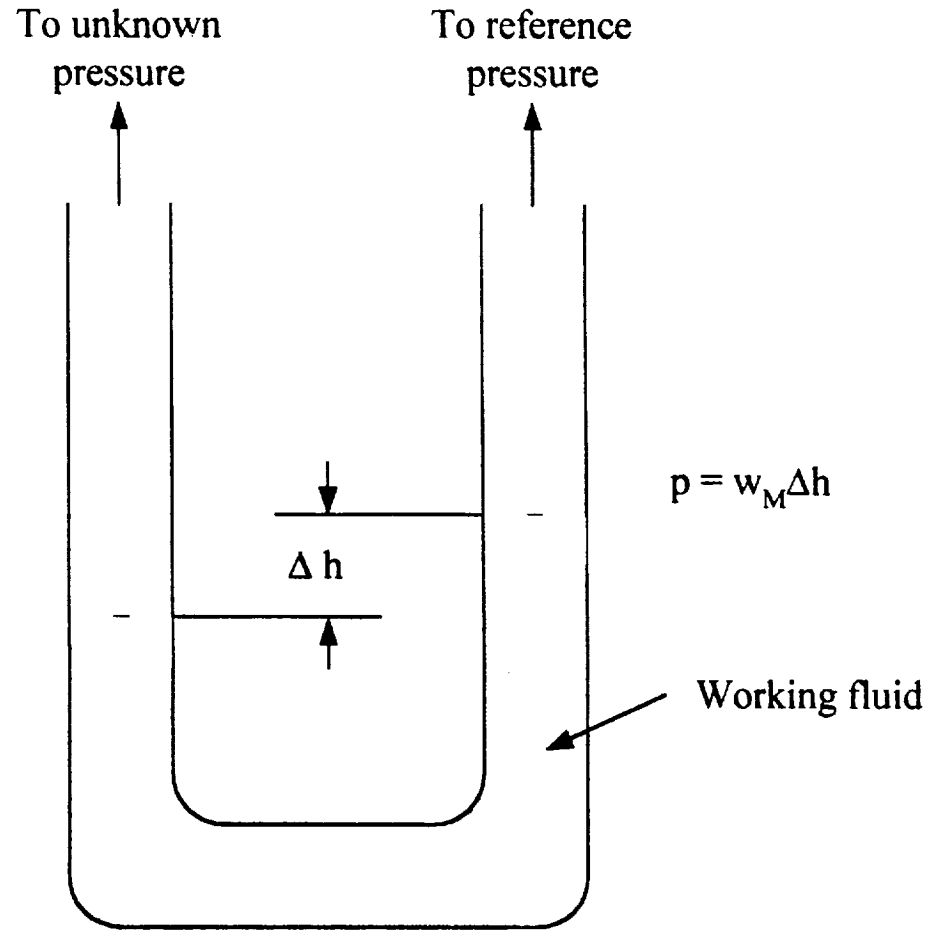

Figure 1. U-tube manometer [5].

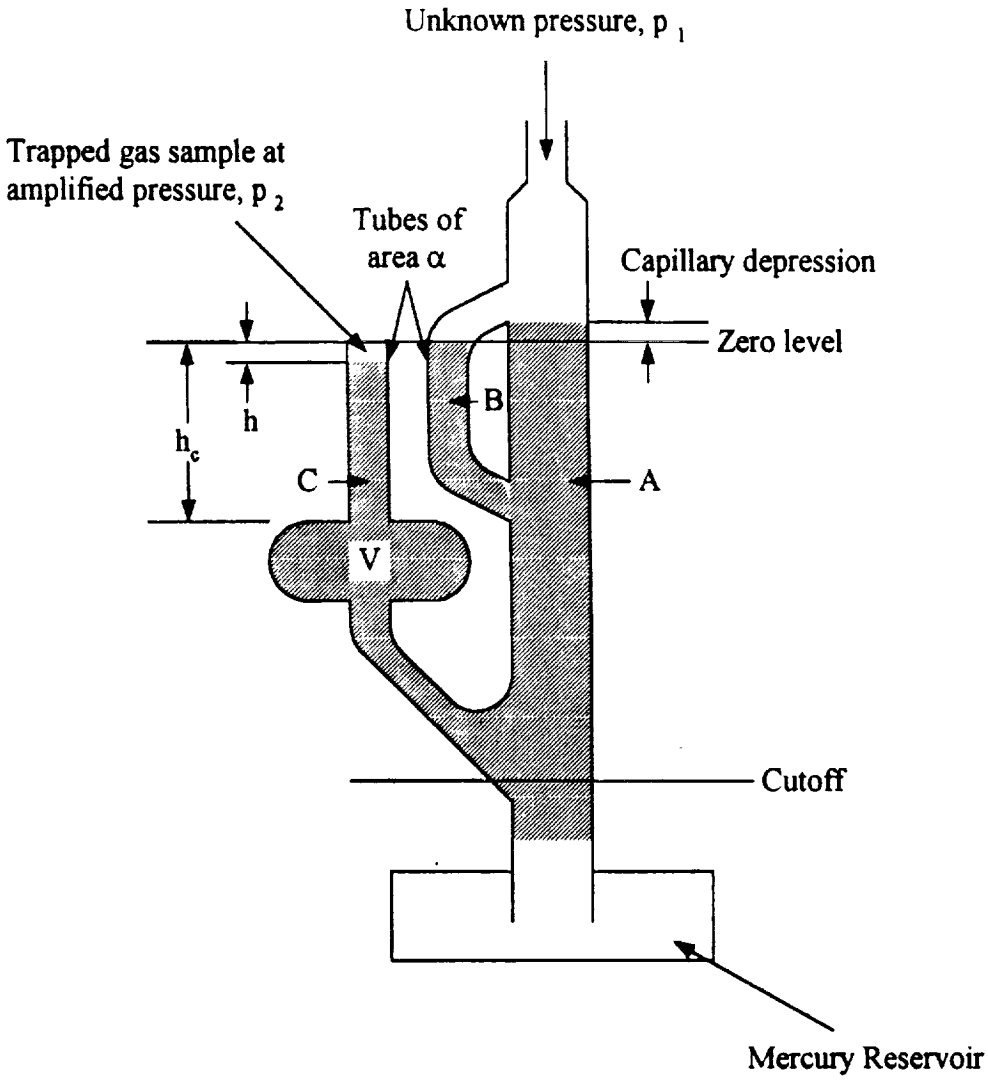

Figure 2. McLeod pressure gauge [1].

and

$$p = \frac{\alpha h^2}{v_1 - \alpha h} \qquad (7)$$

Pressure measurement is accomplished in the Wallace-Tiernan mechanical diaphragm gauge, Figure 3 [8], by admitting an unknown pressure to the hermetically sealed instrument case, where it exerts a pressure on a flat evacuated capsule that has been permanently sealed. Movement of the capsule is transmitted by a lever system to the pointer that registers the pressure on a dial as a pressure above absolute zero.

A variation on the Wallace and Tiernan diaphragm gauge is the capacitive manometer in which diaphragm movement is measured electrically rather than mechanically. Figure 4 [7] shows a cross-section of the gauge head which is comprised of a sealed metal housing, AA, divided into two identical sections by a thin, radially prestressed, metal diaphragm, B. This diaphragm is positioned symmetrically between fixed capacitor plates, C, formed on ceramic discs. This creates a capacitive potential divider in which minute motion of the central diaphragm, following a pressure change, varies the relative capacitance of the diaphragm and the fixed capacitor plates. The plates form part of a bridge circuit, excited by a 10 kHz signal, such that any displacement of the diaphragm unbalances the bridge and produces a 10 kHz signal of amplitude proportional to the pressure. The balanced gauge structure allows for either differential measurements, with pressure changes applied to both sides of the diaphragm, or straightforward pressure measurement against a self-contained vacuum reference by sealing off one side of the diaphragm at high vacuum. The equation governing this

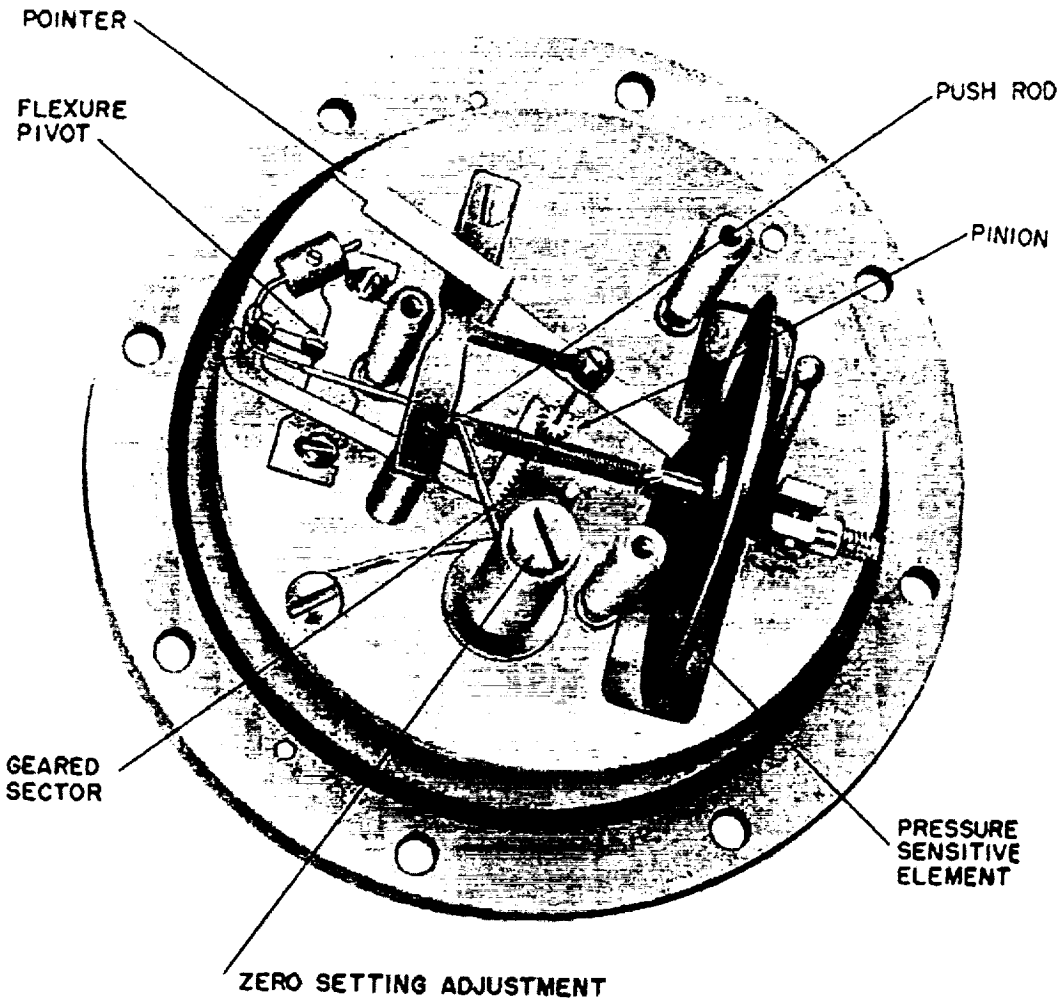

Figure 3. Wallace-Tiernan mechanical diaphragm pressure gauge [8].

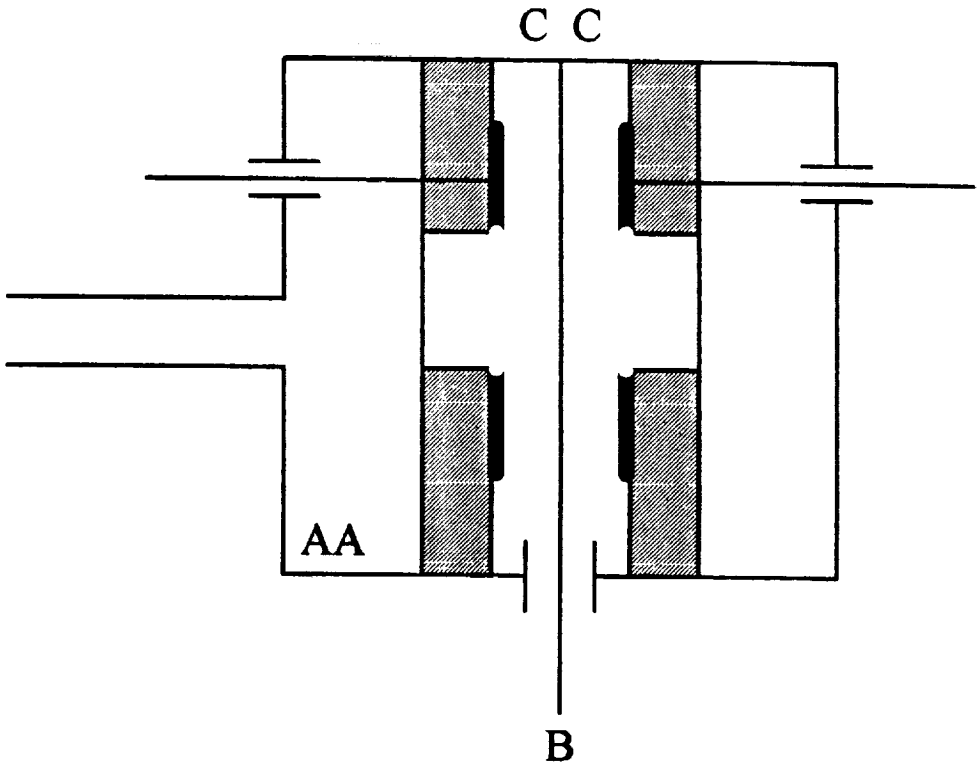

Figure 4. Cross-section through a capacitance manometer [7].

device is

$$p = \frac{C_{output}}{C_{initial}} \tag{8}$$

which yields a linear capacitance variation with pressure.

A sketch of the Knudsen-type pressure gauge is shown in Figure 5. This gauge operates on the principle that a mechanical force is exerted between two surfaces maintained at different temperatures in a gas at low pressure. The two parallel strips, D and E, are placed at a distance apart which is less than the mean free path of the gas molecules. The strip D is at the temperature T_o of the residual gas, while E is maintained at a higher temperature T_1. On the side away from E, D will be bombarded by molecules having root mean square velocity c_o corresponding to the temperature T_o given by

$$c_o = \left(\frac{3RT_o}{M}\right)^{1/2} \tag{9}$$

where R is the universal gas constant and M is the reflection coefficient of the mirror that is used to measure deflection in the same manner as galvanometers. Molecules leaving D will have the same velocity. On the side towards E, however, D will be bombarded by molecules coming from E and will have a higher velocity c_1 corresponding to T_1. As a result, D will receive momentum at a greater rate on the side towards E than on the opposite side, and will experience a torque.

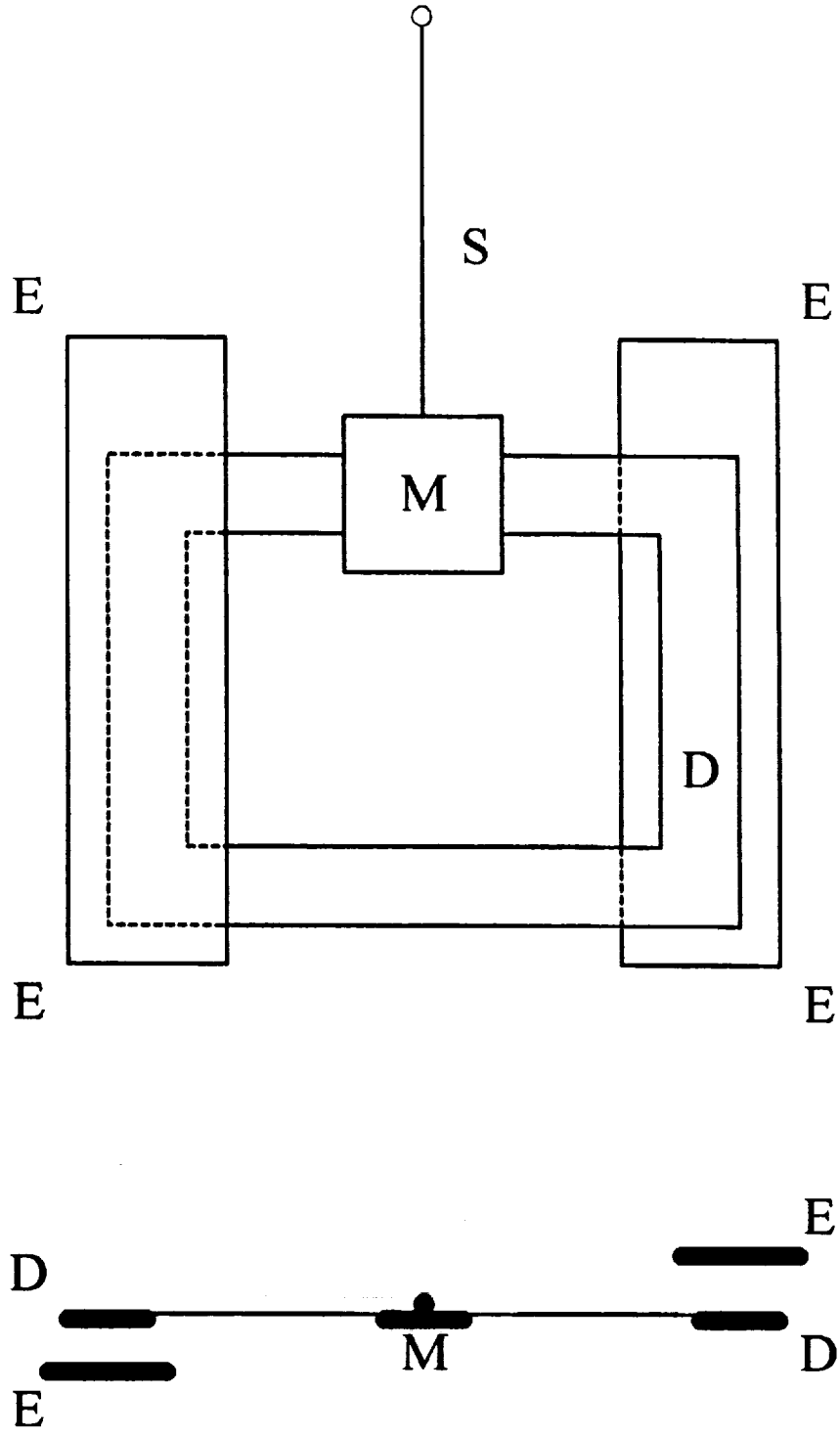

Figure 5. Sketch of Knudsen-type pressure gauge [8].

The net force exerted per unit area, F, is given by the rate at which momentum is is transferred from E to D and is

$$F = \frac{1}{6} nc_o (mc_1 - mc_o) \tag{10}$$

where n is the number of gas molecules per unit volume and m is their mass. In terms of pressure around the strips D and E, the equation is

$$p = 4F\left(\frac{T_o}{T_1 - T_o}\right). \tag{11}$$

If the temperatures T_o and T_1 are maintained constant, then the force, F, is directly proportional to the pressure and is independent of the molecular weight of the gas.

Research has produced many devices over the years to sense changes in pressure, and the term that has been given to these devices is pressure transducer. The essential feature of a pressure transducer is an elastic element that converts energy from the pressure system being investigated to a displacement in the mechanical measuring system. This displacement is converted to a usable pressure output either directly, as in the case of the Wallace-Tiernan pressure gauge, or electrically, as in the case of the capacitance pressure gauge. A diaphragm is the elastic element of the transducers used in these gauges; however, other pressure sensing elements used in transducers include capsules, bellows, straight tubes, and Bourdon tubes [11-15] as illustrated in Figure 6 [13]. Examples of transducers used for pressure measurement include inductive, reluctive, capacitive, piezoelectric, potentiometric, resistive, and strain-gauges [12 - 17]. In recent years, silicon has been used to fabricate pressure transducers/sensors. Along

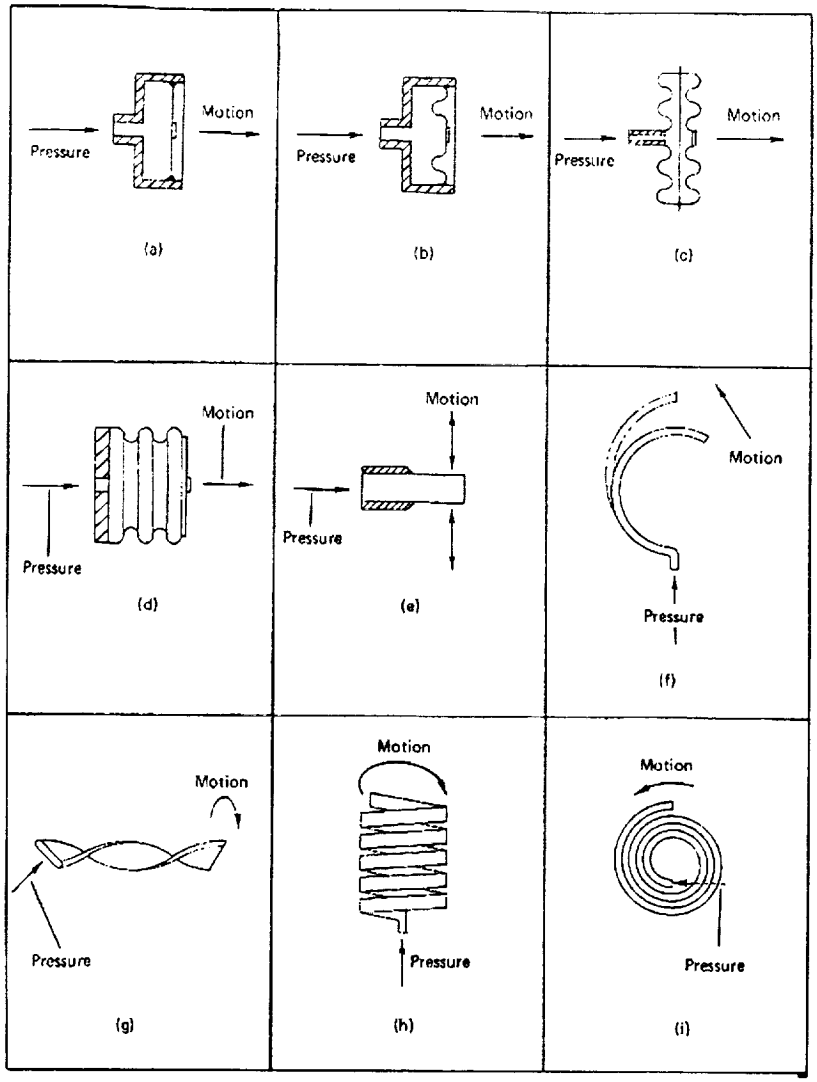

Figure 6. Pressure sensing elements: (a) flat diaphragm; (b) corrugated diaphragm; (c) capsule; (d) bellows; (e) straight tube; (f) C-shaped Bourdon tube; (g) twisted Bourdon tube; (h) helical Bourdon tube; (i) spiral Bourdon tube [13].

with its electrical characteristics, the ability to manufacture very small devices through means other than complex machining makes silicon an attractive material for pressure sensors. The silicon is processed to create a diaphragm which is then configured for use in the different types of pressure sensors.

A fiber optic pressure sensor that uses a diaphragm at the end of a multimode optical fiber has been created for use in the biomedical field [18]. The sensor is placed inside a catheter balloon that is used to dilate the coronary artery, and the pressure inside the balloon is measured optically using the intensity of light reflected off the diaphragm.

Resonant strain gauges have been placed on silicon diaphragms [19] with pressure being measured as a function of the resonator frequency. The frequency is modulated by the strain in the diaphragm surface. In capacitive pressure sensors [20 - 23], the silicon diaphragm is anodically bonded to glass and acts as one of the plates of a parallel plate capacitor. Applying pressure deflects the diaphragm, which in turn causes capacitance variations. A typical structure of a silicon capacitive sensor is shown in Figure 7 [20].

Stress applied to a semiconductor causes a change in the energy gap between the valence band and the conduction band, which affects the number of charge carriers being excited from the valence band to the conduction band, thereby causing a change in the resistivity. This phenomenon is known as the piezoresistance effect [24 - 26] and has been taken advantage of in the fabrication of silicon pressure sensors by diffusing impurity layers on selected areas of the diaphragm. These piezoresistors are arranged in a Wheatstone bridge configuration to compensate for the temperature effects that are known to occur with diffused transducers [27 - 29]. Figure 8 shows a cross-section of the

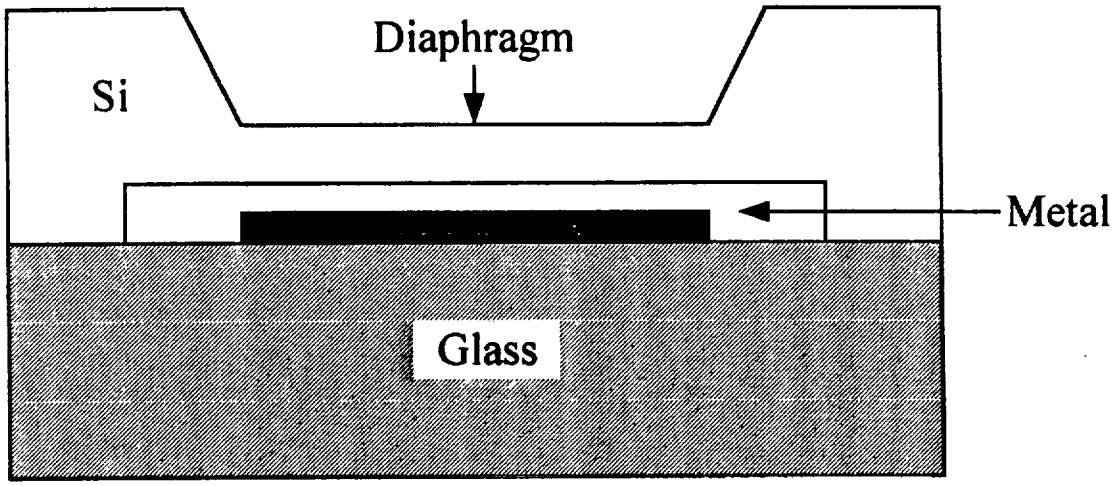

Figure 7. Typical structure of silicon capacitive pressure sensor [20].

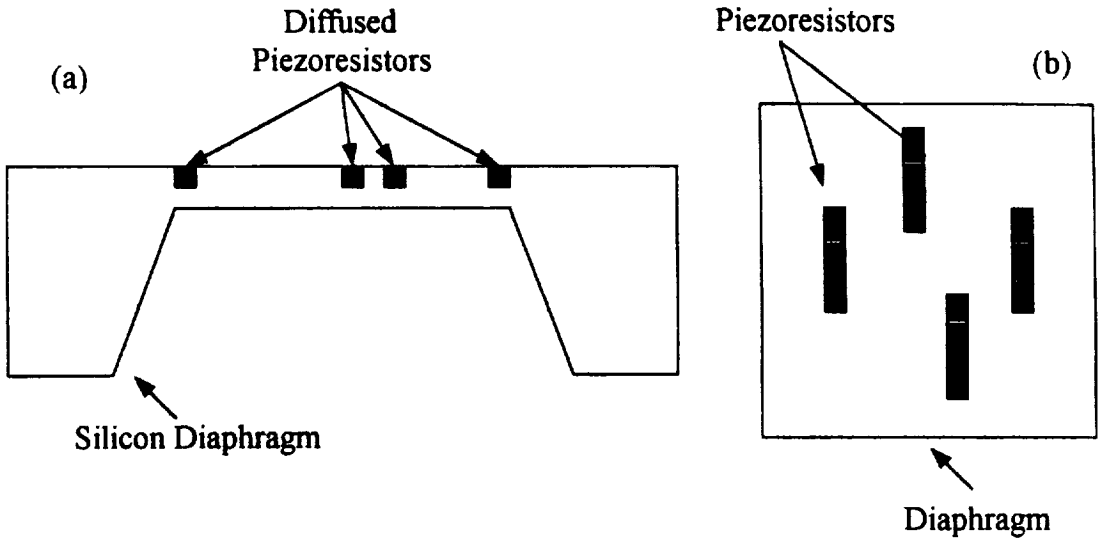

Figure 8.
Schematic of silicon diaphragm with piezoresistors: (a) cross - section; (b) top view [28].

silicon diaphragm with diffused piezoresistors . Other configurations using the piezoresistive effect with the diaphragm as the elastic element have been developed [30 - 37].

Research Goal

A new type of pressure transducer using the diaphragm has been proposed [38, 39]. This sensor is based on the Fowler-Nordheim (F-N) equation for field emission [40]

$$J = \frac{AE^2}{\phi t^2(y)} \exp\left(-B\frac{\phi^{3/2}}{E} v(y)\right) \qquad (12)$$

where $A = 1.54 \times 10^{-6}$, $B = 6.87 \times 10^{7}$, $y = 3.79 \times 10^{-4} E^{1/2}/\varphi$, E is the electric field at the cathode, and φ is the work function of the cathode material. The functions v(y) and t(y) can be approximated by [40]

$$t^2(y) = 1.1 \text{ and } v(y) = 0.95 - y^2. \qquad (13)$$

Silicon can be processed such that an array of sharp tips, known as a field emitter array (FEA), can be formed to serve as the cathode while the diaphragm serves as the anode. A schematic cross-section of this device is shown in Figure 9. The electric field, E, in Equation 12 is a function of the applied voltage, V, and a field conversion factor, β, that takes into account the separation of electrodes and the field enhancement due to the sharp tips of the FEA and is given by [40]

$$E = \beta B . \qquad (14)$$

Operation of this device is such that when pressure is applied, the diaphragm deflects downward toward the array of nano-tips thereby increasing the current according to the

F-N equation. This current can then be related to pressure through calibration. The main advantage of this pressure sensor is that the temperature dependence seen in other pressure sensors is eliminated, as there is no temperature term in the equation for field emission.

Section 2 discusses the theory behind the operation of this field emission based sensor. Section 3 gives the details involved in fabricating a pressure sensor, including the specific aspects of the processing steps needed. Section 4 presents results that have been achieved using this pressure transducer, and Section 5 outlines applications as well as improvements that can be made in the future.

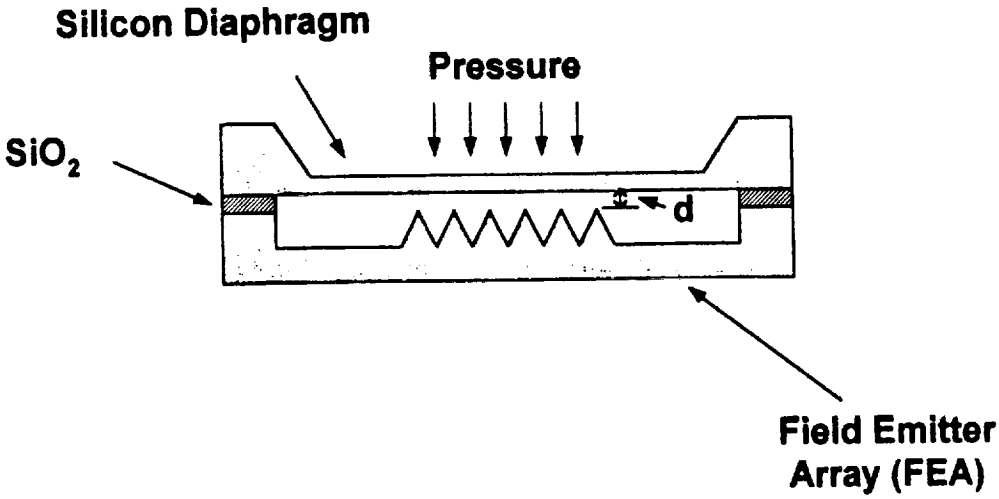

Figure 9. Silicon pressure sensor using an FEA.

II. THEORY OF FIELD EMISSION BASED SENSOR

Concepts of field emission that lead to the Fowler-Nordheim equation are presented in this chapter. The design factors used to determine the thickness and deflection of the diaphragm will be introduced. Finally, a discussion on diamond film and its use in the fabrication of the pressure sensor is included.

2.1 Electron Emission

Electrons can be emitted from the surface of a metal or semiconductor by one of four mechanisms: photo-emission, thermionic emission, Schottky or field-assisted emission, and field emission. The following discussion focuses on metals, but is applicable to semiconductors as well. At the surface of a metal, there exists a potential energy barrier. This is known as the work function, φ, and is defined as the energy required to remove an electron from the Fermi level, E_F, to a position just outside the material (vacuum level) [41]. Photo-emission is the process whereby electrons are emitted by irradiating the metal surface with light of energy $hv \geq \varphi$, where h = Planck's constant and v = light frequency [42, 43]. This effect is used in photo-electric devices.

In thermionic emission, the electrons are given energy by heating the metal/semiconductor. Only those electrons with energies greater than $E_F + \varphi$ which are moving toward the surface will be emitted. The current density of the emitted electrons is given by the equation [42, 43]

$$J = B_e T^2 \exp\left(-\frac{\phi}{kT}\right) \tag{15}$$

where $$B_e = (1 - R)B_o \quad (16)$$

$$B_o = \frac{4\pi e m_e k^2}{h^3} \quad (17)$$

T = Temperature in Kelvin

k = Boltzmann's constant

e = electron charge

m_e = effective mass of an electron.

Equation 15 is the modified form of the Richardson-Dushman equation as it takes into account the wave nature of electrons. As the electrons approach the surface, there is a probability that they will be reflected back into the metal, instead of being emitted over the potential barrier. This is accounted for in B_e using the reflection coefficient, R, which depends on the material and the surface conditions. This type of emission is used in cathode ray tubes and microwave tubes, such as the klystron, UHF triode, and magnetron.

In Schottky emission, an electric field is used to aid the thermionic emission process by lowering the potential energy barrier, φ, as shown in Figure 10 [42]. Inside the metal, an electron is defined as having zero potential energy (PE), i.e., all of its energy is kinetic. Just outside the surface, the electron experiences a force from the positive charge created when it was emitted (Figure 10a). An applied field causes a PE gradient just outside the surface(Figure 10b). The total PE is the sum (Figure 10c). The PE barrier is thereby effectively reduced in the presence of an applied field to ($E_F + \varphi_{eff}$), where φ_{eff} is a new effective work function that takes the field effect into account and is

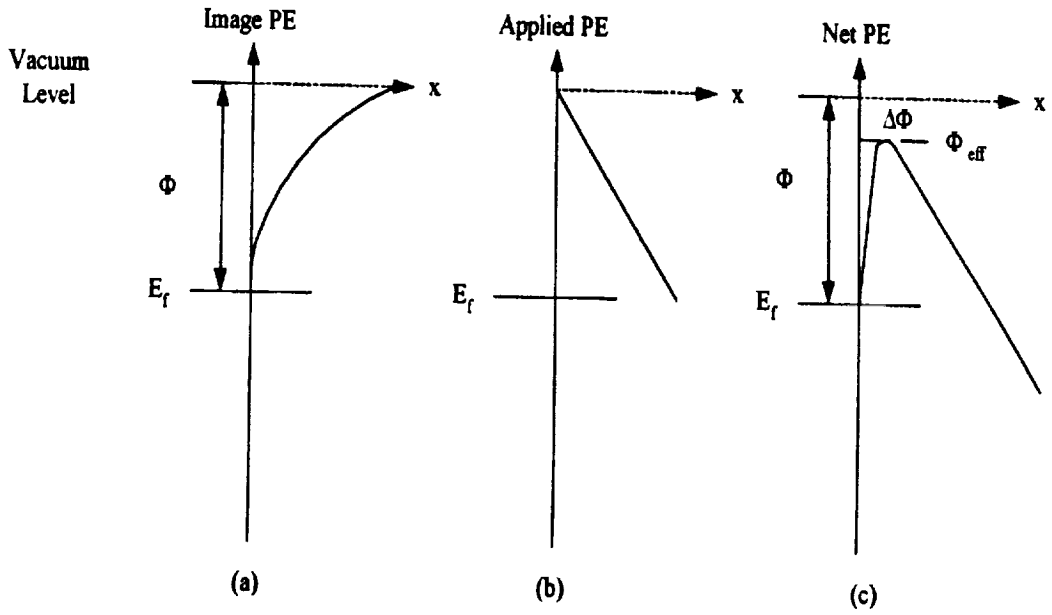

Figure 10.
PE diagram: (a) PE of an electron near the surface of a conductor or semiconductor; (b) Electron PE due to an applied field; (c) The overall PE is the sum of (a) and (b) [42].

given by

$$\phi_{eff} = \phi - \left[\frac{e^3 E}{4\pi\varepsilon_o}\right] \tag{18}$$

where ε_o is the absolute permittivity. This lowering of the work function by the applied field is known as the Schottky effect. The current density is given by the Richardson-Dushman equation, but with ϕ_{eff} instead of ϕ:

$$J = B_e T^2 \exp\left[\frac{-\left(\phi - \beta E^{1/2}\right)}{kT}\right] \tag{19}$$

where

$$\beta_s = \left(\frac{e^3}{4\pi\varepsilon_o}\right)^{1/2} = 3.79x10^{-5}\frac{eV}{\sqrt{Vm^{-1}}} \tag{20}$$

is the Schottky coefficient. Field-assisted thermionic emission is used in metal-semiconductor contacts [41].

The different types of emission that have been described thus far require that the electrons gain enough energy to overcome the potential energy barrier. When the field becomes very large ($E > 10^7$ V cm^{-1}), however, the potential barrier becomes very narrow, and there is a definite probability that an electron at energy E_F will tunnel through the barrier and escape into vacuum [42 - 47]. This is known as field emission, and the theory behind it was developed by L. W. Nordheim and R. H. Fowler in 1928 [43, 44], with the result being the well-known Fowler-Nordheim (F-N) equation.

Figure 11 illustrates the tunneling situation. When a field, E, is applied to a metal surface, electrons of kinetic energy, $(KE)_x$, along the emission direction see a barrier of height $E_F + \phi - (KE)_x$ and width $X_F = (E_F + \phi - (KE)_x)/Ee$. If this is thin and low enough, transmission will occur with finite probability.

Tunneling is a quantum-mechanical phenomenon with no classical analogue. The Heisenberg uncertainty principle allows us to relate the uncertainty, Δx, in the position and the uncertainty, Δp_x, in the momentum of the electron by

$$\Delta p \Delta x \approx \hbar / 2 . \qquad (21)$$

If electrons near the Fermi level are taken into consideration, the pertinent uncertainty in momentum, $(2m\phi)^{1/2}$, corresponds to the barrier height ϕ. The corresponding uncertainty in position is

$$\Delta x \approx \frac{\hbar}{2(2m\phi)^{1/2}} . \qquad (22)$$

The barrier width is

$$x = \frac{\phi}{Ee} . \qquad (23)$$

There will be a good chance of finding an electron on either side of the barrier if

$$\frac{\phi}{Ee} \approx \frac{\hbar}{2(2m\phi)^{1/2}} \qquad (24)$$

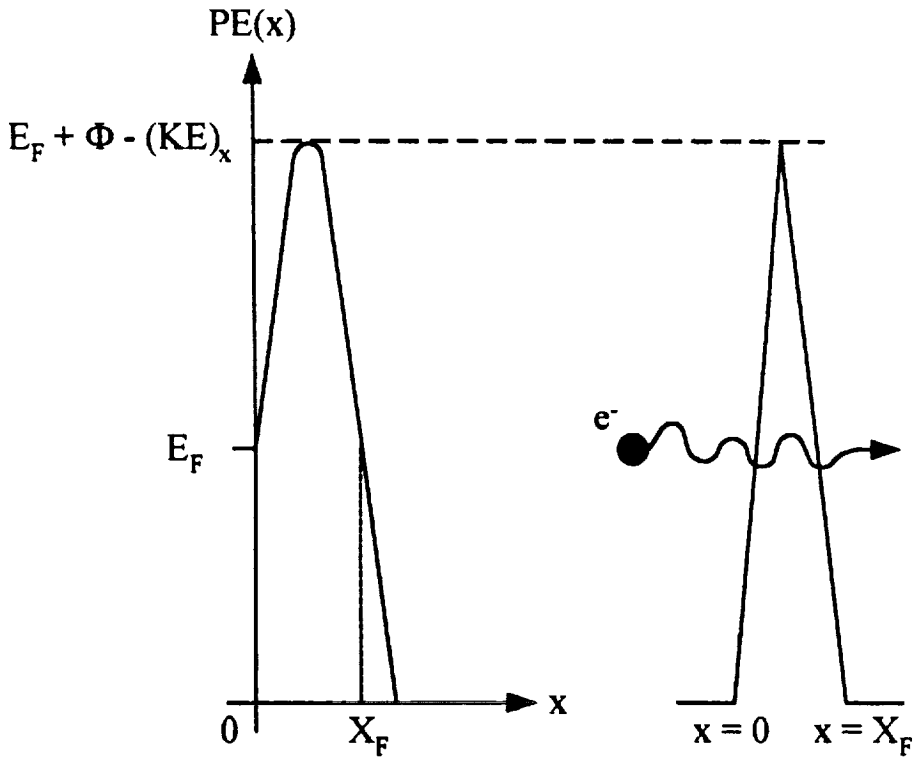

Figure 11. Electron tunneling through the potential barrier.

or

$$2\left(\frac{2m}{\hbar^2}\right)^{1/2}\frac{\phi^{3/2}}{Ee}\approx 1. \qquad (25)$$

The condition in Equation 25 is roughly that required for field emission.

Consider a one-dimensional barrier with a height of V_o, as shown in Figure 12. The transmission coefficient can be found using the Wentzel-Kramers-Brillouin (WKB) method [47]. The result is

$$T(KE,V_o)=T\ \exp\left[-2\left(\frac{2m}{\hbar^2}\right)^{1/2}\int_o^a\left(V-KE\right)^{1/2}dx\right] \qquad (26)$$

where T(KE, V_o) is the probability that an electron traveling to the right will not be reflected at the barrier but will proceed through it. KE is the electron's kinetic energy. T_o is a function of KE and V_o and is given by

$$T_o=\frac{16E(V_o-KE)}{V_o^2} \qquad (27)$$

and is usually approximated by a constant of unity.

The exponential part of T can be demonstrated using the following simple argument. T will roughly be equal to

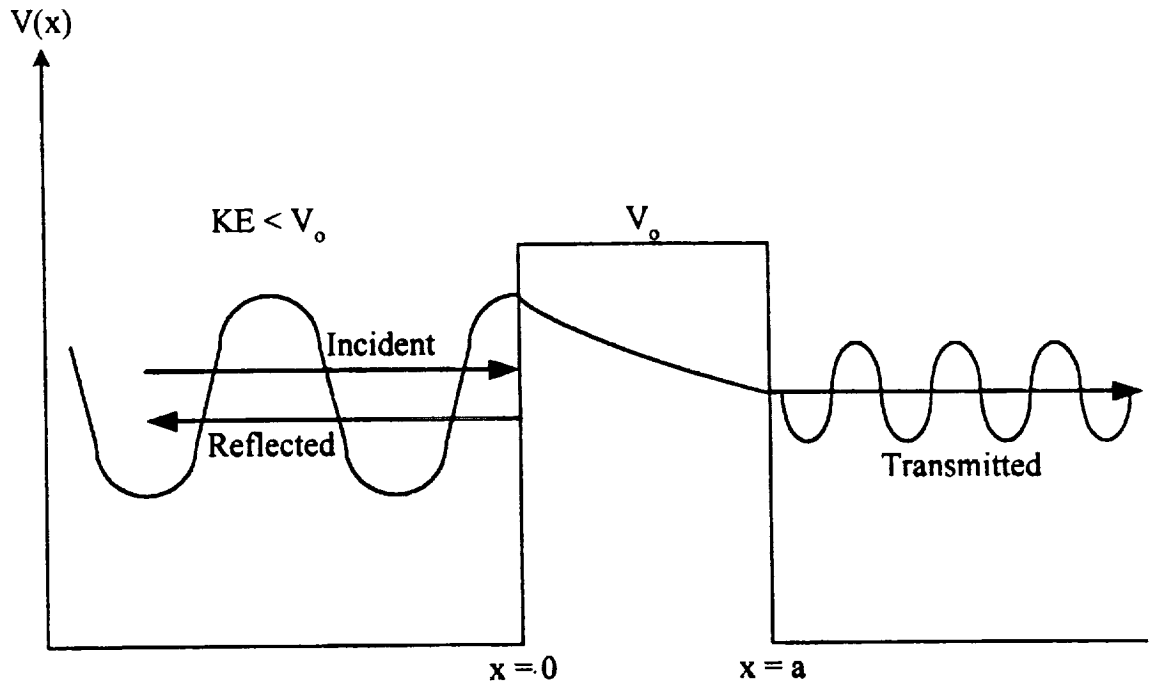

Figure 12. Tunneling transmission coefficient [42].

$$T \approx \left[\frac{\psi(a)}{\psi(o)}\right]^2 \tag{28}$$

where $\psi(a)$ and $\psi(0)$ are the electron wave functions at x = a and x = 0, respectively. Over an infinitesimal distance, dx, ψ can be approximated by $\exp(jk_1x)$, where k_1 is

$$k_1 = \frac{p}{\hbar} = \left[\frac{(KE - V_o)2m}{\hbar^2}\right]^{1/2}. \tag{29}$$

In the barrier region, $(KE - V_{o})$ is negative so that

$$\psi = \exp\left[-\left(\frac{2m}{\hbar^2}\right)^{1/2}(V_o - KE)^{1/2}x\right]. \tag{30}$$

Hence

$$\frac{\psi(x+dx)}{\psi(x)} = \exp\left[-\left(\frac{2m}{\hbar^2}\right)^{1/2}(V_o - KE)^{1/2}dx\right] \tag{31}$$

and

$$\frac{\psi(a)}{\psi(o)} = \exp\left[-\left(\frac{2m}{\hbar^2}\right)^{1/2}\int_0^a (V_o - KE)^{1/2}dx\right] \tag{32}$$

so that

$$T \approx \exp\left[-\left(\frac{2m}{\hbar^2}\right)^{1/2}\int_0^a (V_o - KE)^{1/2}\,dx\right]. \qquad (33)$$

The exponential term on the right hand side of Equation 26 can be interpreted by looking at Figure 11. Excluding the factor $2(2m/\hbar^2)^{1/2}$, it represents the area under the curve with ordinate $(V_o - KE)^{1/2}$ from x = 0 to x = X_F. This area is very close to being triangular in shape, with base $(E_F + \phi - (KE)_x)/Ee$ and height $(E_F + \phi - (KE)_x)^{1/2}$, so that

$$Area \approx \frac{1}{2}\frac{[E_F+\phi-(KE)_x]^{3/2}}{Ee}. \qquad (34)$$

Substitution into Equation 26 yields

$$T = f[(KE)_x, V_o \exp\left[-\left(\frac{2m}{\hbar^2}\right)^{1/2}\left(\frac{[E_F+\phi-(KE)_x]^{3/2}}{Ee}\right)\right]. \qquad (35)$$

This is very similar to T calculated more rigorously by Fowler and Nordheim [43]:

$$\frac{4[(KE)_x(\phi + E_F - (KE)_x]^{1/2}}{} \exp\left[-\frac{4}{3}\left(\frac{2m}{\hbar^2}\right)^{1/2}\left(\frac{[E_F+\phi-(KE)_x]^{3/2}}{Ee}\right)\right]. \qquad (36)$$

If the electrons are limited to an energy of E_F, Equation 36 gives

$$T = \frac{4(\phi E_F)^{1/2}}{\phi + E_F} \exp\left[--6.8x10^7 \frac{\phi^{3/2}}{E} \right] \qquad (37)$$

with ϕ in electron volts and E in volts per centimeter. An approximation of the current density can be found by multiplying Equation 37 by the total rate of arrival of electrons. A more accurate current density is found by using Equation 36 for the transmission probability, multiplying by the appropriate differential arrival rate, and integrating over $0 \leq (KE)_x \leq E_F$. The result is the Fowler-Nordheim equation [43]

$$J = 6.2x10^6 \frac{(E_F/\phi)^{3/2}}{E_F + \phi} E^2 \exp\left(-6.8x10^7 \frac{\phi^{3/2}}{E} \right) \qquad (38)$$

for all energies in electron volts and E in volts per centimeter.

Equation 38 is the Fowler-Nordheim equation for field emission from the surface of a metal without accounting for the image effect. To compensate for this, a multiplicative correction factor must be included in the equations [44 - 47]. This correction factor is

$$\alpha = (1 - y)^{1/2} \qquad (39)$$

where

$$y = \frac{3.8x10^{-4}E}{\phi}. \tag{40}$$

Thus, the Fowler-Nordheim equation becomes

$$J = 6.2x10^{6}\frac{(E_F/\phi)^{1/2}}{\alpha^2(\phi + E_F)}E^2 \exp\left(\frac{-6.8x10^{7}\phi^{3/2}\alpha}{E}\right). \tag{41}$$

In a metal, the Fermi level coincides with the highest filled state at 0° K and changes only very slightly at moderate temperatures. In an intrinsic semiconductor, the Fermi level lies approximately at the middle of the energy gap [41]. When impurities are added to a semiconductor, they either donate an electron to the conduction band creating n-type material, or donate a hole to the valence band, i.e., the impurity accepts an electron from the semiconductor, creating a p-type material. The Fermi level compensates for the increases in either holes or electrons by moving closer to the conduction band for n-type semiconductors or closer to the valence band for p-type semiconductors.

A complex mathematical analysis for field emission from semiconductors was conducted by Robert Stratton [48] in 1961. Others [42, 47] have explained this process in a simplified form. The electrons that are emitted from a semiconductor come from either the valence band or the conduction band that comprise what are known as surface states. Under the presence of an applied field, the electrons work their way from the

interior of the semiconductor to these surface states and make themselves available for emission. These electrons still must tunnel through a potential barrier, but the electrons in the conduction band of the surface states require less energy than those in the valence band because the potential barrier is smaller.

There are two separate cases for field emission from a semiconductor: emission from the conduction band and emission from the valence band. The equation that governs emission from the valence band is the F-N equation, but the work function must be modified. The effective work function is [47]

$$\phi_{valence} = \chi + E_g \tag{42}$$

where χ is the electron affinity or the energy required to move an electron from the bottom of the conduction band into vacuum. Also, since the applied field needed for emission from the valence band is higher than that required for emission from the conduction band, the image correction is appreciable. This is given by the Nordheim factor, α, but with an argument [47]

$$y = \left(\frac{\varepsilon - 1}{\varepsilon + 1}\right)^{1/2} 3.6x10^{-4} \frac{E^{1/2}}{\chi + E_g} \tag{43}$$

where ε is the dielectric constant of the semiconductor.

When emission is from the conduction band, if the field does not penetrate into the interior of the semiconductor (Figure 13 [47]), the rate at which the electrons strike the surface from the interior is

$$n\left(\frac{kT}{2\pi m}\right)^{1/2}\frac{electrons}{cm^2 s} \tag{44}$$

and the emission current is

$$J=\frac{2nekt}{(\pi m\chi)^{1/2}}\exp\left(\frac{-6.8x10^7\chi^{3/2}}{E}\right) \tag{45}$$

where n is the electron density in the conduction band. The average kinetic energy of electrons in the emission direction has been taken as ½ kT « χ. The number n is given by either

$$n=2\left(\frac{2\pi mkT}{h^2}\right)^{3/2}\exp\left(\frac{-E_g}{2kT}\right) \tag{46}$$

for intrinsic semiconductors or

$$n=N^{1/2}2^{1/2}\left(\frac{2\pi mkT}{h^2}\right)^{3/4}\exp\left(\frac{-E_i}{2kT}\right) \tag{47}$$

for doped semiconductors where N is the total number of donors per unit volume. In the case where there is no field penetration, the total current is temperature dependent.

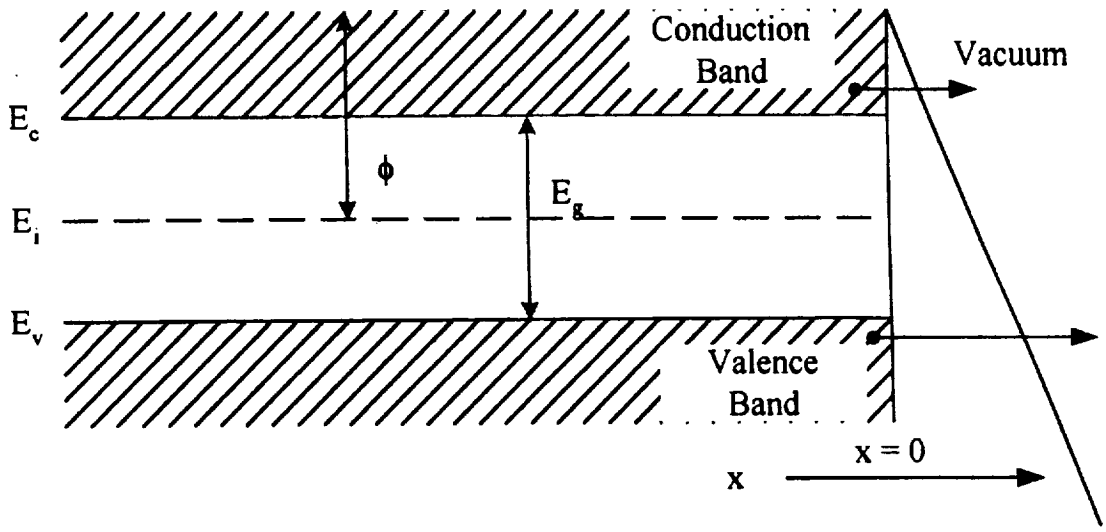

Figure 13. Electron emission through potential barrier for a semiconductor [47].

When field penetration into the interior of the semiconductor does occur, as is usually the case, the bands bend to compensate, as shown in Figure 14. Physically, this corresponds to the existence of a distributed, excess volume charge of electrons near the surface and a neutralization of the normally ionized donor impurities in this region. If the conduction band is deformed by an energy v_o, which is not sufficient to bring it below the Fermi level, Boltzmann statistics will still apply and the emission current density will be given by Equation 45 multiplied by a factor $\exp(-v_O/kT)$ representing the increased electron concentration at the bottom of the band. The work function remains the same as in the case of no field penetration.

Since the Fermi level is usually close to the undeformed conduction band when there are donor impurities and since the applied field is high, the bottom of the band will generally dip below E_F in n-type material. A pool of electrons will collect in this depression. These electrons obey Fermi statistics. The highest filled level of this pool coincides with the Fermi level. The work function in the Fowler-Nordheim exponent will be decreased by $E_F - V1_O$, i.e.,

$$\phi_{effective} = \phi - \left(E - v_o\right) \tag{48}$$

where

$$E_F - v_o = \gamma E^{4/5} \tag{49}$$

and

$$\gamma = 4.5x10^{-7}\varepsilon^{-2/5} \tag{50}$$

for E in volts cm^{-1} and energies in electron volts.

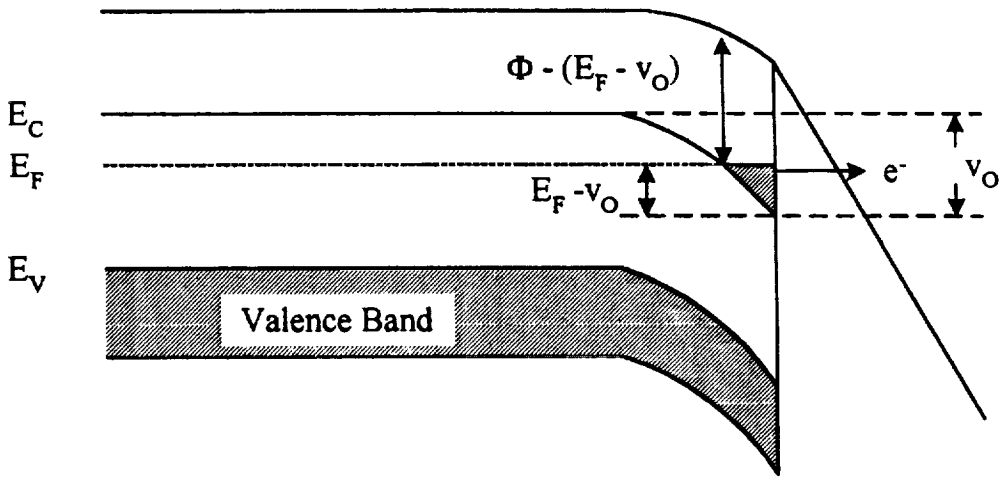

Figure 14.
Field emission through potential barrier with field penetration into the interior of the semiconductor [47].

The preceding discussion indicates that field emission from semiconductors will be temperature independent, either if it comes from the valence band, or if there is sufficient field penetration to lower the conduction band at the surface below the Fermi level. In all other cases, there will be an exponential temperature dependence.

It should be noted that the theory presented here for field emission is for flat surfaces, and the applied field needs to be quite large for electrons to be emitted. Research has shown [40, 49 - 51] that machining the metal or semiconductor into sharp points or tips locally enhances the electric field thereby reducing the voltage needed for field emission to occur. This has resulted in modifications to the Fowler-Nordheim equation, but leaving the basic principles intact. The result of these modifications is Equation 12, repeated here for continuity.

$$J = \frac{AE^2}{\phi t^2(y)} \exp\left(\frac{-B\phi^{3/2} v(y)}{E}\right) \qquad (12)$$

2.2 Silicon Diaphragm

When a uniform pressure is exerted, the diaphragm is deflected downward towards the field emitter array, and the current density increases according to the Fowler-Nordheim equation. Figure 15 shows a diagram of the current density as a function of diaphragm distance from the array. A maximum change in current density for a small change in distance is a desired parameter of the pressure transducer operation. The diaphragm is constructed from silicon, which is placed on top of the field

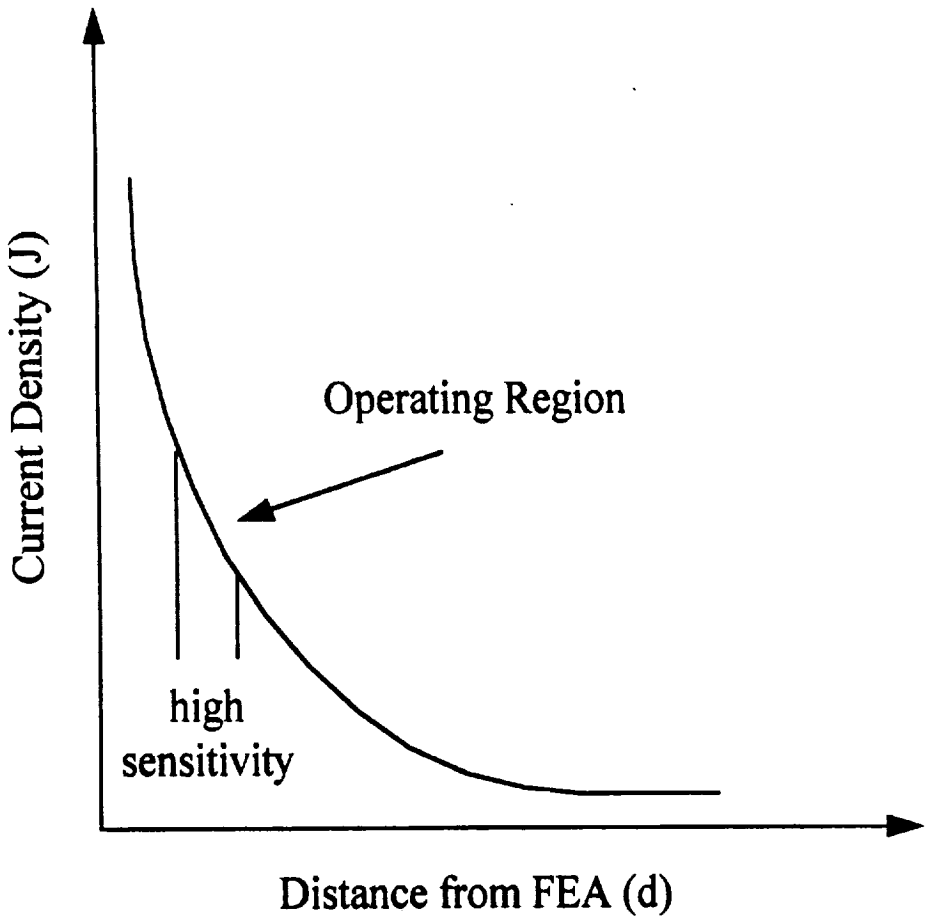

Figure 15. Current density versus diaphragm separation from the FEA.

emitter array as shown in Figure 9. The diaphragm is essentially a flat plate with all the edges fixed. This configuration has a maximum deflection given by [52]

$$d = -\frac{1.407x10^{-7}\, pl^4}{Yt^3} \tag{51}$$

where p = pressure in Pascals

l = length of the sides of the diaphragm

Y = Young's modulus of the material in kg cm^{-2}

t = thickness of the diaphragm in meters

and the negative sign accounts for the downward deflection of the diaphragm.

It was decided in the early stages of research that the pressure sensor should be able to be integrated into digital circuits; this meant that the voltage placed on the sensor should not be more than 5 volts. In order to obtain a sufficient field for emission using this voltage, the spacing between the diaphragm and the array should be very small, while at the same time allowing for deflection over a range of pressures without damaging the emitters. It was decided that the transducer should be able to cover a range of 20 pounds per square inch or from atmosphere (1.013×10^5 Pa) to 2.392×10^5 Pa. The spacing between the diaphragm and the FEA required to produce a usable current density without any deflection and a 5 volt source is 1.5×10^{-6} meters.

Since the equation for deflection has 3 variables and only one of them had been decided upon, one other variable had to be accounted for so that a solution for the third could be found. The FEA occupies a space of 0.4 mm x 0.4 mm, and the diaphragm has to cover this space with the center being over the top of the array. The diaphragm was chosen to be square with dimensions of 4 mm x 4 mm.

Using the spacing between the diaphragm and the array, the thickness was calculated to be 174 μm. This thickness would cause the diaphragm to rest on top of the FEA at the high end of the pressure range, possibly causing damage. Therefore, a diaphragm thickness had to be determined that would allow for maximum sensitivity and proper device operation. Plots of deflection vs. pressure for various diaphragm thicknesses over the desired pressure range are shown in Figure 16. From the figure, it can be seen that a diaphragm thickness between 175 μm and 180 μm would satisfy the parameters mentioned.

Equation 51 is valid if the sensor is sealed in vacuum. However, if the device is sealed in air or some other gas at atmospheric pressure, there will be a pressure exerted from the inside of the device back against the diaphragm when an external pressure is applied, and this must be accounted for in calculating the thickness of the diaphragm. At a constant temperature, the gas law PV=nRT, which is a constant, can be used to calculate the pressure inside the sensor with a decrease in the volume due to the action of the external pressure applied. The initial pressure and volume are known, so the constant can be determined. The deflection equation is modified to allow for the pressure inside the device and becomes

$$d = -\frac{1.407x10^{-7}\left(p_{external} - p_{internal}\right)l^4}{Yt^3} \qquad (52)$$

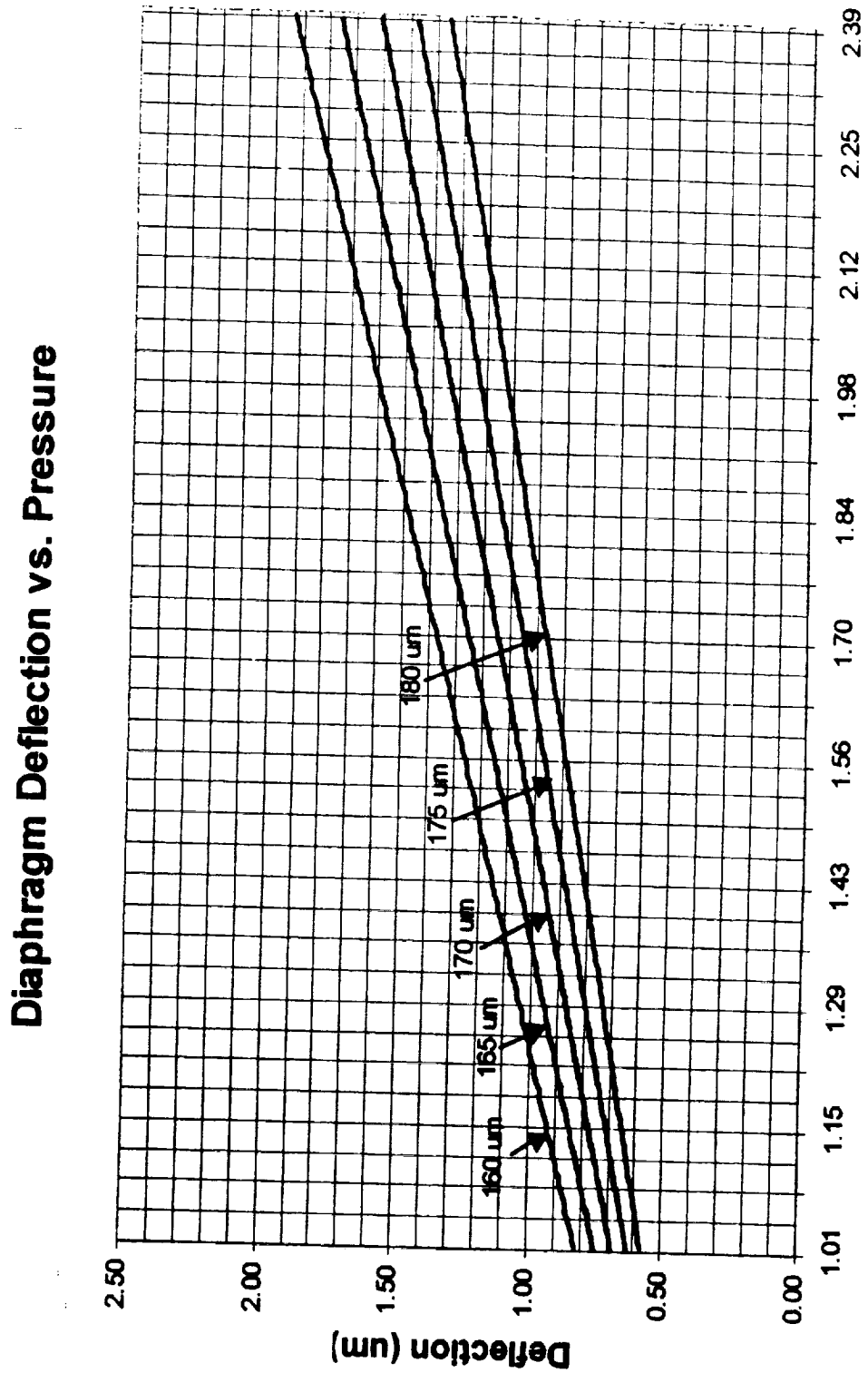

Figure 16. Diaphragm deflection versus pressure for various thicknesses.

where

$$p_{internal} = \frac{p_o V_o}{V_o - 2.55x10^{-6}\pi d} \tag{53}$$

and p_o and V_o are the initial pressure and volume inside the device, respectively. Many iterations of this equation have been calculated, and the optimum thickness for a diaphragm sealed at atmospheric pressure with a gas inside was found to be between 135 μm and 140 μm.

2.3 Theoretical Analysis

A plot of current density as a function of diaphragm distance from the FEA is shown in Figure 17 using Equation 12. The diaphragm thickness used to calculate the deflection is 175 μm. Following Zhirnov, et. al. [51], the field enhancement factor is calculated by

$$\beta = \frac{h}{rd} \tag{54}$$

where h and r are the height and radius, respectively, of the nano-tips that make up the FEA, and d is the distance between the FEA and the diaphragm. The Microelectronics Research Laboratory at Old Dominion University has found typical values of h = 2.20 μm and r = 20 nm [76]. A diamond film coating is grown on the FEA to further enhance emission which increases the radius to 50 nm. The work function of the diamond has been calculated to be 1.08 eV [76]. The applied voltage used in the equation is 5 volts.

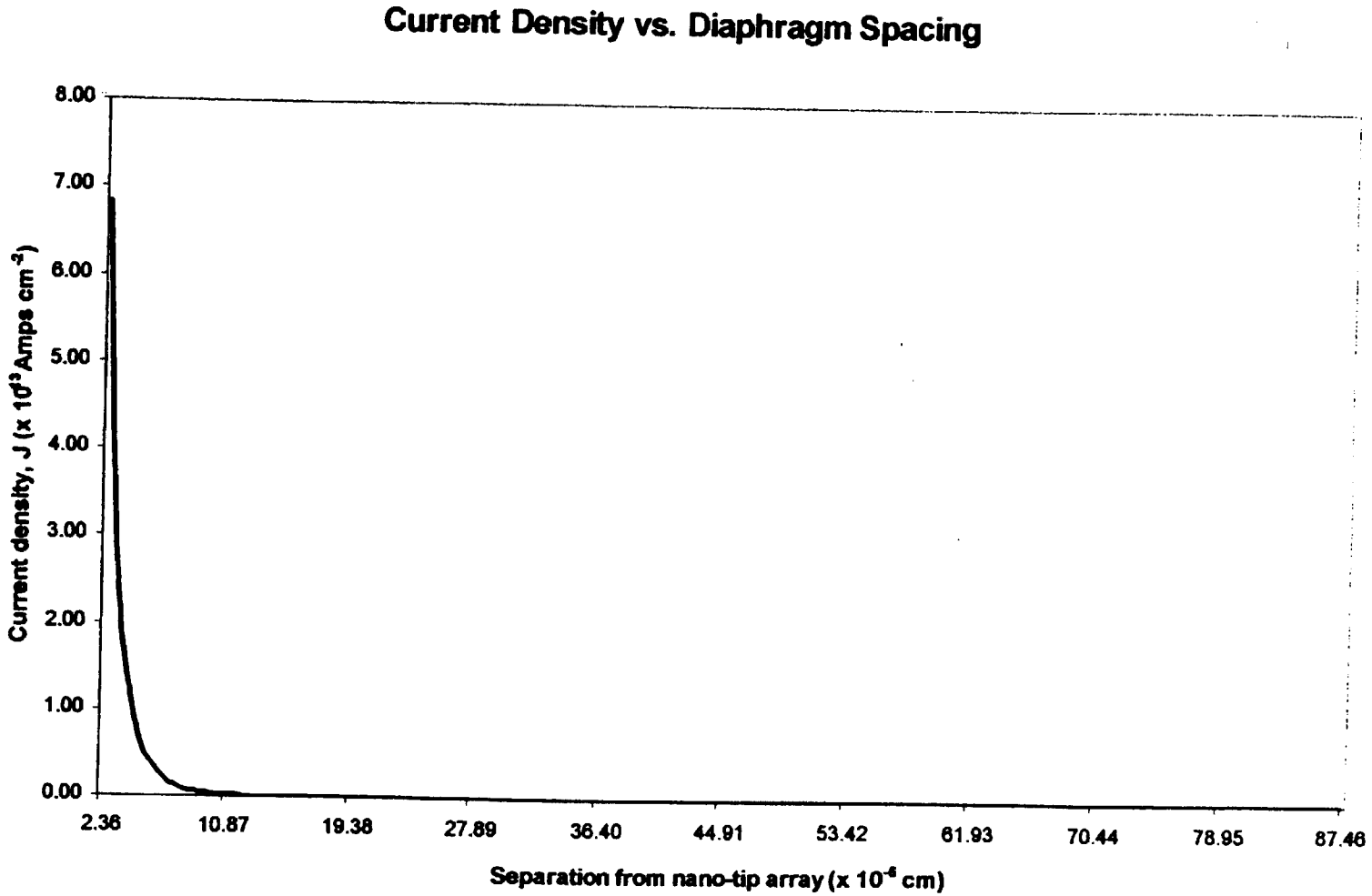

Figure 17. Current density as a function of the diaphragm spacing from the FEA.

2.4 Diamond as an Emitter

Diamond has been studied for many years now. Diamond has many physical properties, such as high thermal conductivity, high physical strength, and chemical inertness that industry has taken advantage of. Synthetic diamond is used as a material in cutting tools. Diamond is also used as a heat sink in high power devices. In addition to its physical properties, diamond has electrical properties that make it attractive as a candidate for use in electronic devices. Diamond has been classified as a wide bandgap semiconductor with high electron and hole mobilities. Table 2 lists many of the properties of diamond [53, 54].

In recent years diamond has been studied extensively for use in field emission. One of the properties of diamond is its low or negative electron affinity [55, 56]. In addition to the other properties of diamond, this property makes diamond especially attractive for use as a field emitter. Diamond thin films have been successfully deposited on various substrates using a variety of methods. These methods include combustion flame deposition, Hot Filament Chemical Vapor Deposition (HFCVD), and Microwave Plasma Chemical Vapor Deposition (MPCVD). The different substrates used for deposition have been molded into various shapes, the most common being the form of a pyramid. Composition of the gases that are used in growing diamond have been examined to determine the mixture facilitating diamond growth and subsequent emission. While some substrate configurations and gas mixtures produce better results than others, the literature suggests that if diamond growth is achieved, the result is a lower turn-on voltage for field emission [51, 55 - 76].

Table 2: Properties of Diamond.

Crystal Structure	Diamond
Lattice Constant	3.567 A
Energy Gap	5.46 eV
Effective conduction band density of states	~ 10^{20} cm^{-3}
Effective valence band density of states	~ 10^{19} cm^{-3}
Breakdown field	10^{6} - 10^{7} V cm^{-1}
Electron mobility	2200 cm^{2} V^{-1} s^{-1}
Hole mobility	1800 cm^{2} V^{-1} s^{-1}
Melting point	4373° C @ 125 kbar
Thermal conductivity	20 W cm^{-1} $°C^{-1}$
Hardness	10000 kg mm^{-2}
Coefficient of friction (dynamic)	0.03
Dielectric constant	5.7
Dielectric strength	10^{7} V cm^{-1}
Resistivity	10^{13} - 10^{16} ohm-cm
Work function	negative on [111] surface

III. EXPERIMENTS

The pressure sensor is fabricated by placing two structures, the diaphragm and the nano-tip array, together and bonding them. This section will explain the details of the fabrication process for each. The processing of silicon involves cleaning, oxidation, lithography, etching, re-oxidation, and in the case of the nano-tip array, diamond nucleation and growth. After bonding, two leads are attached to the device and it is mounted inside a pressure chamber for testing, the specifics of which will also be explained.

3.1 Processing Steps

The processing steps used to create the diaphragm and the nano-tip array differ only slightly for each structure.

3.1.1 Cleaning

Before any processing can be done to a silicon substrate, a thorough cleaning of the surface is a must if a viable device is to be produced. A cleaning sequence that has been generally adopted proceeds in the following manner [77]:

(1) Remove gross organics and particulates.

(2) Remove organic films.

(3) Remove native surface oxide.

(4) Remove all traces of cleaning solutions and all particulates from the surface.

Removal of gross organics and particulates, which include dust and any semiconductor particles left over from polishing the wafer or cutting of the wafer, is done by rinsing

with deionized water (DIH_2O). The sample is placed in a solution of sulfuric acid (H_2SO_4) and hydrogen peroxide (H_2O_2), which has been heated to 120° C, and is ultrasonically agitated for a period of 2 minutes to remove any additional organics that were not removed by step (1). The sample is rinsed in DIH_2O and dipped in a 2.5% solution of hydroflouric acid to remove any native surface oxide, after which it is rinsed and dried.

3.1.2 Oxidation

Silicon dioxide has several uses: to serve as a mask against implantation or diffusion of dopant into silicon, to provide surface passivation, to isolate one device from another, to act as an insulator in MOS structures, and to provide electrical isolation of multi-level metallization systems [78]. There are a number of techniques which have been developed for forming oxide layers, such as thermal oxidation, wet anodization, vapor-phase technique (chemical vapor deposition (CVD)), and plasma anodization or oxidation [41, 77, 78].

Thermal oxidation is the technique used in the fabrication of the pressure sensor. There are two types of thermal oxidation: wet and dry. While both produce silicon dioxide (SiO_2), the time required for each to produce the same thickness of oxide differs greatly. Dry thermal oxidation is frequently used when very thin oxides are required. Wet thermal oxidation produces thicker oxides at a faster rate and is the method used in the manufacturing of the pressure sensor.

Wet thermal oxidation is accomplished by bubbling oxygen through water held near the boiling point; this steam-oxygen mixture is then flowed over the sample that has

been placed in a furnace heated to 1000° C. Figure 18 shows a schematic diagram of the horizontal oxidation furnace and bubbling system. Oxidation proceeds according to the following reaction [41, 77, 78]:

$$Si + 2H_2O \rightarrow SiO_2 + 2H_2 \tag{55}$$

This reaction occurs at the surface of the substrate and is linear at the initial stages of oxide growth. However, as the oxide is formed, the oxidant must diffuse through the oxide that has already grown to get to the surface of the silicon so that a reaction can take place, hence, oxide growth proceeds at a parabolic rate. The thickness of oxide grown over a period of time can be determined using the Deal-Grove model, developed by B. E. Deal and A. S. Grove in 1965 [41, 77, 78]. This model states that the thickness of an oxide grown is governed by the linear-parabolic equation:

$$d_o^2 + Td_o = Z(t + \tau) \tag{56}$$

where

$$T = 2D\left[\frac{1}{k_s} + \frac{1}{h}\right] \tag{57}$$

$$Z = \frac{2DC^*}{N_1} \tag{58}$$

$$\tau = \frac{d_i^2 + Td_i}{Z}. \tag{59}$$

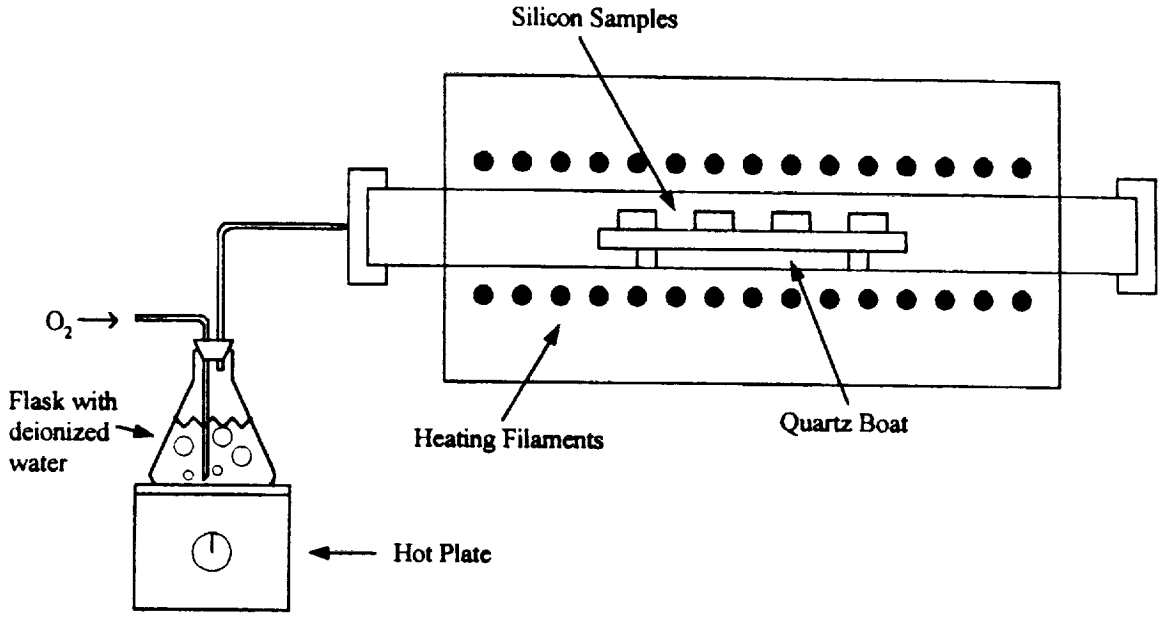

Figure 18. Schematic of horizontal oxidation furnace and bubbling system.

Here, D is the diffusion coefficient; h is the gas-phase mass-transfer coefficient in terms of concentration in the solid, given by h = HkT, where H is Henry's law constant; k_s is the rate constant of chemical surface reaction for silicon oxidation; $C^* = Hp_G$, where p_G is the partial pressure in the bulk of the gas; N_1 is defined as the number of oxidant molecules incorporated into a unit volume of the oxide layer; and τ represents a shift in the time coordinate to account for the presence of the initial oxide layer d_i. Equation 56 can be solved for the amount of time needed to grow an oxide layer of desired thickness, and vice-versa. B is known as the parabolic rate constant and the quantity B/A is known as the linear rate constant. The constants A and B have been calculated for various temperatures and can be found in Table 3 [78]. Figure 19 shows a graph of oxide thickness versus time using wet oxidation at a temperature of 1000° C.

Table 3. Rate constants for wet oxidation of silicon [78].

Oxidation temperature (°C)	T (μm)	Parabolic rate constant Z (μm²/h)	Linear rate constant Z/T (μm/h)	τ(h)
1200	0.05	0.720	14.40	0
1100	0.11	0.510	4.64	0
1000	0.226	0.287	1.27	0
920	0.50	0.203	0.406	0

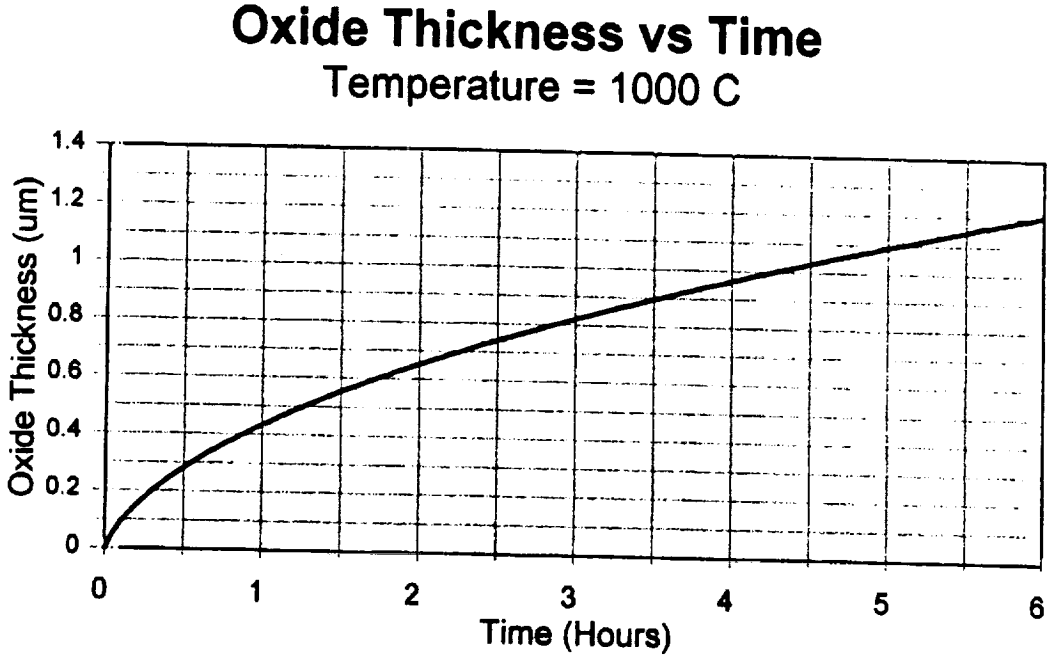

Figure 19. Wet thermal oxide thickness versus oxidation time.

The Deal-Grove model is a very useful tool for predicting the thickness of oxide grown, but slight deviations from this model are found due to factors such as geographic location, type of furnace used, etc. Experiments conducted at Old Dominion University have shown that oxide thicknesses are slightly less (tenths of a μm) than those predicted.

3.1.3 Lithography

Lithography is the process of transferring patterns of geometric shapes on a mask to a thin layer of radiation-sensitive material, known as resist, covering the surface of a silicon sample [41, 77, 78]. The lithographic process can be accomplished by various techniques, but optical lithography is primarily used. Optical lithography uses a resist which is sensitive to ultraviolet light, hence it is named photoresist. Two types of photoresist are available: positive and negative. Positive resists allow the exposed areas to be removed whereas negative resists allow the unexposed areas to be removed. Figure 20 depicts the lithographic process and the effect of using positive resist.

The first step in the lithography process is to coat the sample with a thin layer of photoresist by placing the sample on a spinner and holding it in place through the use of a vacuum pump. Enough photoresist is applied to cover the sample which is then spun at 4500 rpm for 40 seconds to thin out the resist and ensure surface coverage is uniform. The sample is placed on a hotplate set at 95° C to harden the photoresist.

Next, the mask is placed in contact with the sample using a mask aligner, and both are exposed with ultraviolet light. The intensity of the ultraviolet light and thickness of the photoresist determines the length of time needed for exposure, usually between 1 and 5 minutes. The sample is then placed in a bath of developer, causing the exposed portions of the photoresist to be washed away, revealing the oxide. The sample

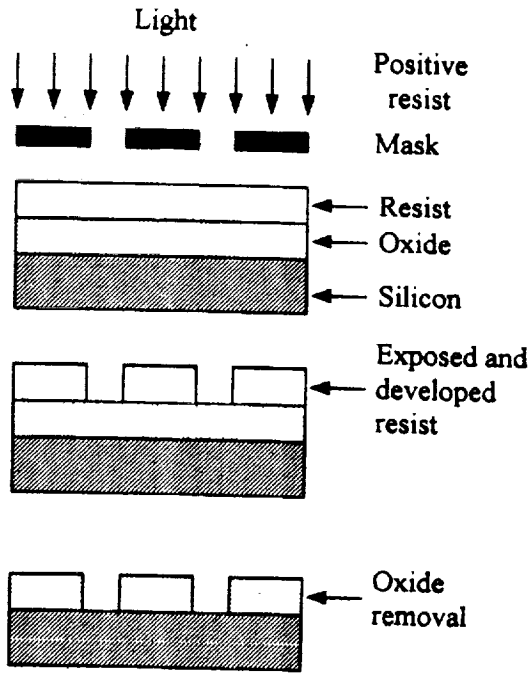

Figure 20. Lithography process and the effect of positive resist [77].

is rinsed, dried, and baked again to ensure that the photoresist is properly set before proceeding.

The unwanted oxide is removed by immersing the sample in a bath of buffered hydrofluoric acid (BHF) consisting of 5 parts DIH_2O to 1 part concentrated hydrofluoric acid for a period of time such that bare silicon is exposed. This depends on the thickness of the oxide and the etch rate of the acid, which is ~ 12 μm per minute. The resist used to mask the oxide is removed, and the sample is rinsed and dried.

3.1.4 Orientation Dependent Etching

Etching is the process of removing unwanted layers of material and creating a structure that can be used for various devices depending on the application. There are many different kinds of etching. These include wet chemical, electrochemical, plasma etching, reactive ion etching (RIE), ion beam milling, and high temperature vapor etching [77]. Wet etching, in which the sample is immersed in an aqueous etching solution, is the oldest and least expensive form of etching. There are two types of wet etching: anisotropic or orientation dependent etching (ODE) and isotropic etching. Orientation dependent wet etching is the form of etching that is used in the fabrication of the pressure sensor.

Orientation dependent wet etching is the process of preferential directional etching of silicon [41, 77]. One of the basic features of anisotropic etchants is that etch rates are strongly dependent on crystallographic orientation and atomic bond strengths. Structures that are etched with anisotropic etchants are bounded predominately by (111) planes, i.e., the (111) planes are the slowest etching planes [79 -81]. As an example, a commonly used orientation dependent etch for silicon consists of a mixture of potassium

hydroxide (KOH) in water and isopropyl alcohol. The etch rate is 0.6 μm/min for the (100) plane, 0.1 μm/min for the (110) plane, and only 0.006 μm/min (60 A/min) for the (111) plane at 80° C; thus the ratio of the etch rates for (100), (110), and (111) planes is 100:16:1 [41].

The (100) plane is the fastest etching plane due to the fact that the (100) plane has the least number of atoms/cm^2 as well as being less densely packed than other planes used in processing, i.e. the (110) plane and (111) plane [41, 42, 77]. Figure 21 shows a cubic cell of the diamond lattice that makes up silicon with the (100) plane shaded. The number of atoms per square centimeter on the (100) plane is equal to the number of atoms cut by the plane divided by the area of the plane. The (100) plane has four shared atoms at the corners and one unshared atom at the center. The lattice parameter, a, is 0.543 nm for silicon, and the total number of atoms per square centimeter on the (100) plane is:

$$n_{<100>} = \frac{4*\frac{1}{4}+1}{(5.43x10^{-8})^2} = 6.783x10^{14}\,\frac{atoms}{cm^2} \quad . \qquad (60)$$

Figure 22 shows the cubic cell with the (110) plane shaded. The (110) plane has four atoms at the corners shared with neighboring planes (each contributing 1/4), two atoms on the upper and lower sides shared with upper and lower planes (each contributing ½), and two atoms within the plane all by themselves. Using the lattice parameter, a, the total number of atoms per square centimeter on the (110) plane is:

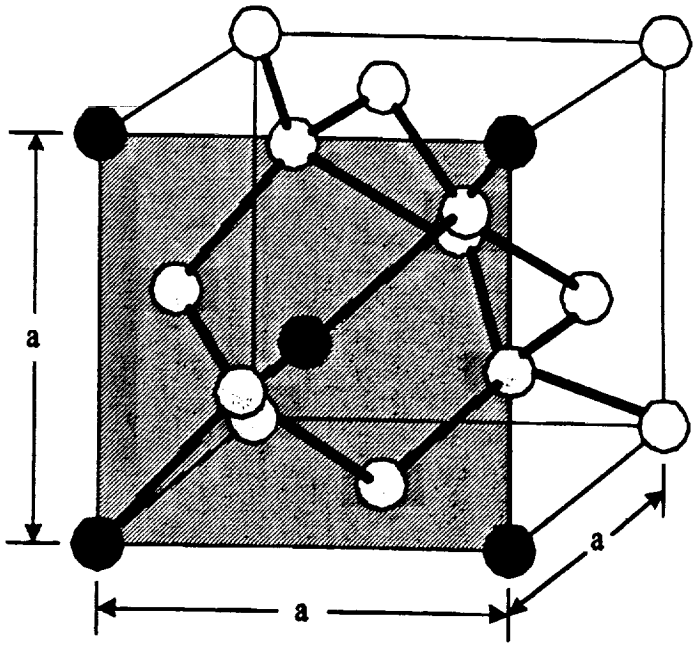

Figure 21. Cubic cell of diamond lattice with (100) plane.

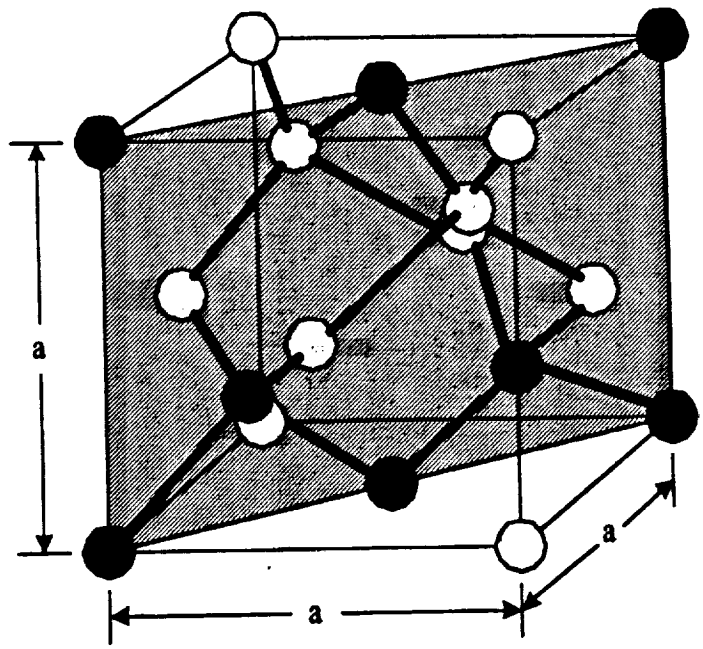

Figure 22. Cubic cell of diamond lattice with (110) plane.

$$n_{<110>} = \frac{4*\frac{1}{4}+2*\frac{1}{2}+2}{(5{,}43x10^{-8})^2 * \sqrt{2}} = 9.5928x10^{14}\,\frac{atoms}{cm^2}. \qquad (61)$$

Figure 23 shows the cubic cell with the (111) plane shaded. The (111) plane has three shared atoms in each corner (each contributing 1/6 of an atom) and three atoms on each or its sides (each contributing ½). This leads to a total number of atoms on the (111) plane being:

$$n_{<111>} = \frac{3*\frac{1}{6}+3*\frac{1}{2}}{\frac{(5.43x10^{-8})^2 * \sqrt{12}}{4}} = 7.8325x10^{14}\,\frac{atoms}{cm^2}. \qquad (62)$$

It is easy to see that the (100) plane has the least number of atoms per square centimeter when compared with the (110) and (111) planes, thus, this plane is the fastest etching plane. When comparing the (110) and (111) planes, the (110) plane has a higher density of atoms than the (111) plane, yet it etches faster than the (111) plane. The (111) plane has stronger bonds between atoms than the (110) plane, hence the (111) plane etches slower than all other planes.

Since the (111) plane is the slowest etching of all the planes used in processing, it is used as an "etch stop". Orientation dependent etching of (100) oriented silicon

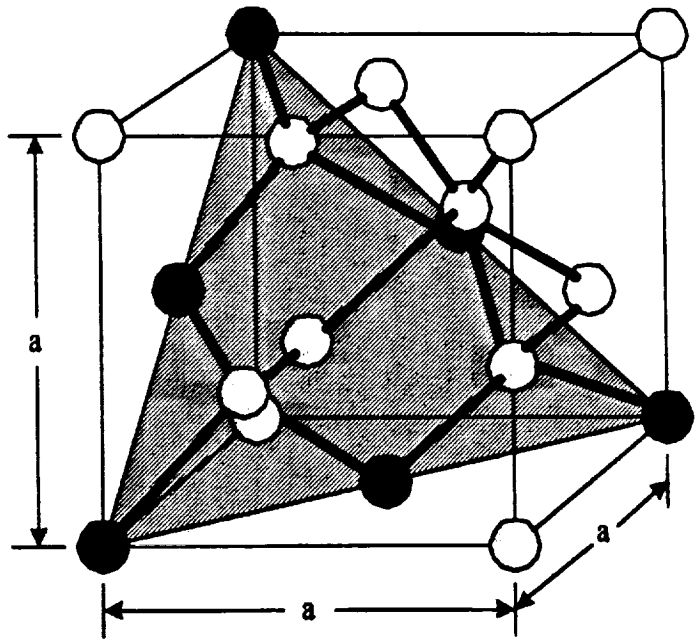

Figure 23. Cubic cell of diamond lattice with (111) plane.

through a patterned silicon dioxide mask will produce V-shaped grooves, the edges being (111) planes at an angle of 54.7° from the (100) surface as shown in Figure 24 [82]. Figure 25 [77] shows the relationship of width and depth with respect to the mask opening.

3.2 Device Fabrication

The processing steps described in the previous section were used to create the two structures, the nano-tip array and the diaphragm, that make up the pressure sensor. This section discusses the fabrication of each structure and how they were placed together to create an operational pressure sensor. Diamond growth on the nano-tip array will also be addressed.

3.2.1 Nano-tip Array

The nano-tip array begins as a (100) oriented silicon wafer. In the early stages of research, the wafer was cut into 9 mm X 9 mm sample sizes, but as research progressed, whole 2" wafers were processed. Regardless of whether samples or wafers are used, the fabrication of the array is the same. The samples were cleaned using the H_2SO_4-H_2O_2 cleaning solution and ultrasonic agitation as previously described. A 30 minute oxide was then grown on the silicon. This produced ~ 0.3 μm of SiO_2, which acts as a mask while etching the silicon into the sharp tips of the array. Patterns were defined by photolithography; the mask used is comprised of 400 (10 μm X 10 μm) squares, as shown in Figure 26. These 400 squares are arranged such that an array of 20 x 20 squares is created. The spacing between the centers of the squares is 20 μm. This pattern was transferred to the photoresist and subsequently to the oxide by etching in BHF.

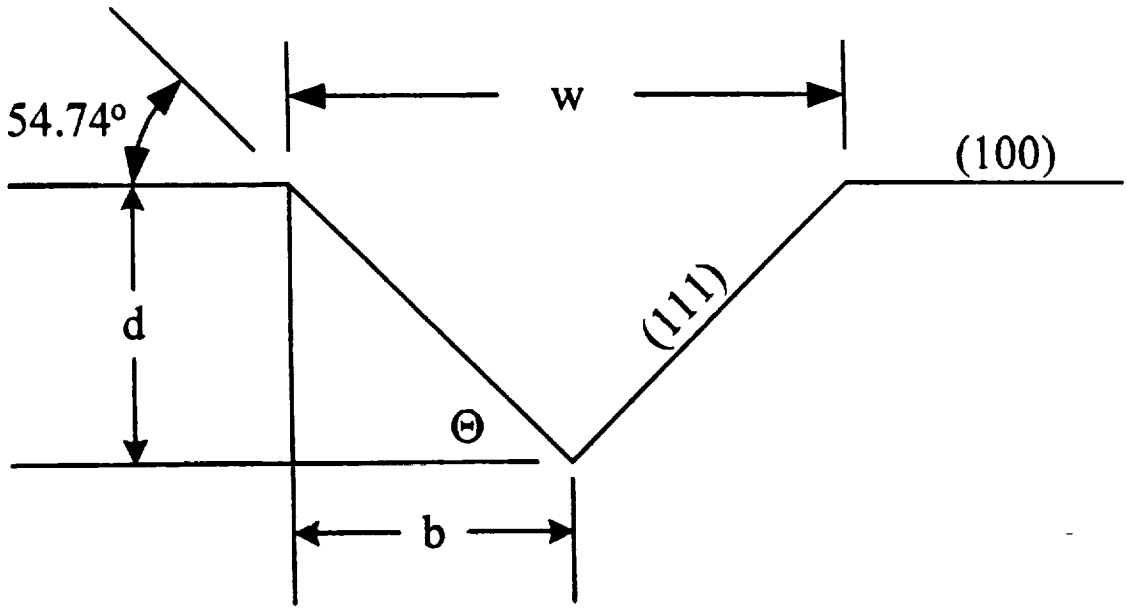

$$w = 2b = \frac{2d}{\tan\theta} = \frac{2d}{\tan 54.74^\circ} = \frac{2d}{1.4} \qquad (63)$$

Figure 24. Etching feature with respect to mask opening of (100) plane [77].

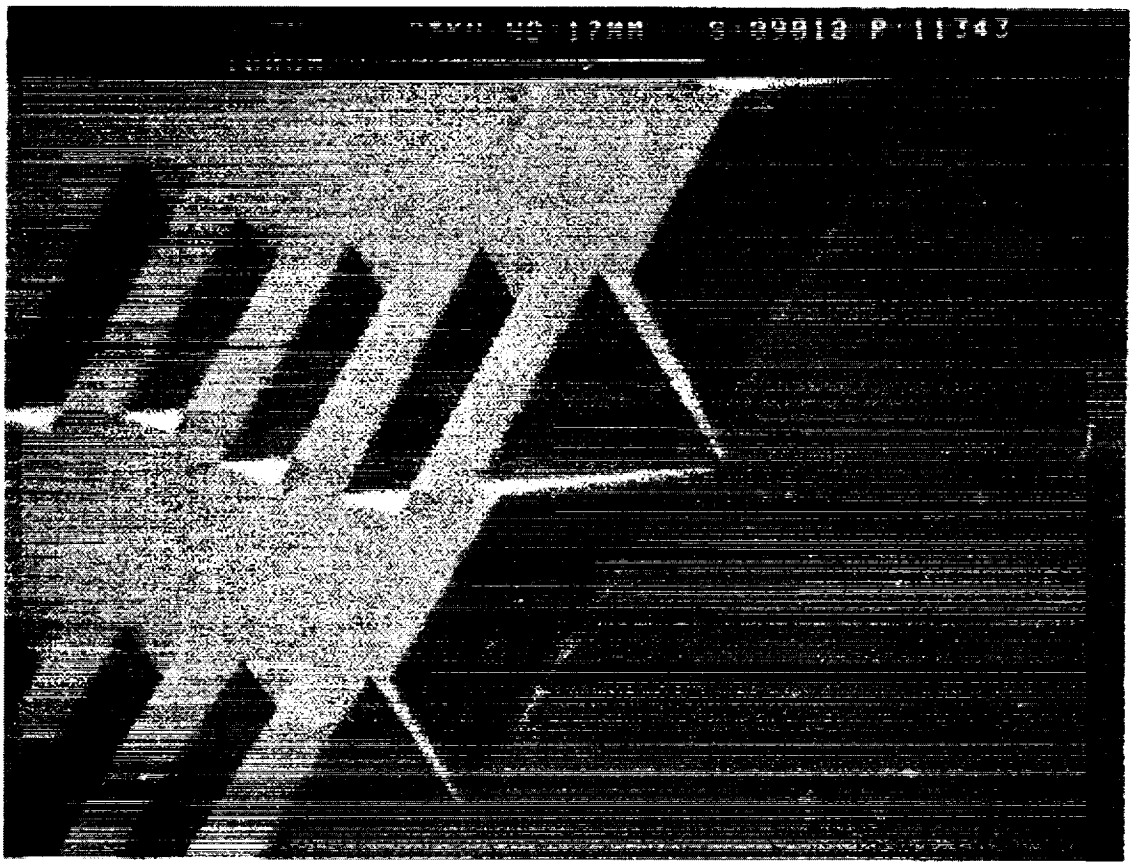

Figure 25.
Orientation dependent etching of (100) plane through patterned SiO_2 mask [82].

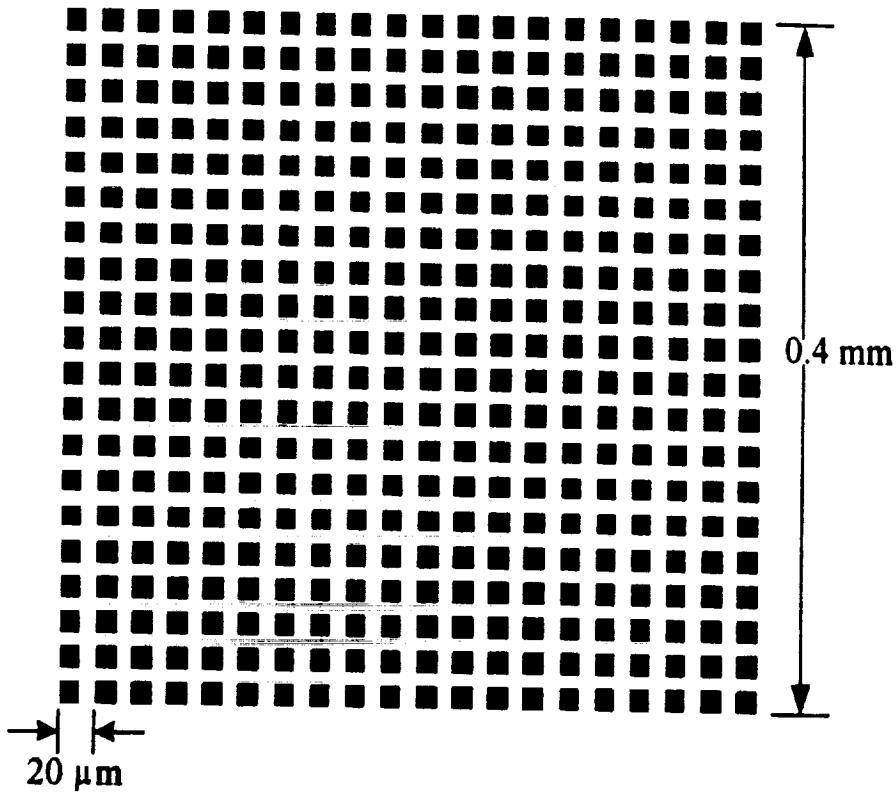

Figure 26. Mask used to create nano-tip array.

Tetramethylammonium hydroxide (TMAH) was used as the etchant for the silicon samples. TMAH is an anisotropic etchant that is more widely used in industry because it is more environmentally friendly than other etchants and leaves less residue on the silicon during the etching process as it contains no metal ions (like the potassium present in KOH) [82 - 86]. In order to produce the sharpest tips possible, the etching must be monitored. TMAH possesses the property that as the concentration is increased, the etch rate decreases. An observable etch rate is achieved using a concentration of ~ 40% TMAH heated to ~ 95° C. As the etchant begins reacting, the surface of the exposed silicon, (100) plane, is etched away. Lateral etching also takes place proceeding towards the (111) plane of the silicon under the oxide mask; this is known as undercutting. The oxide mask acts to prevent the TMAH from vertically etching the (100) plane that is directly beneath the oxide squares. The TMAH continues to etch the silicon from all sides until a point is reached where the oxide square or cap falls off leaving a sharp point or tip in the silicon. The time required to completely etch the nano-tip array was approximately 8 minutes. Figure 27 shows schematically the process used to create the array. Etching progress was monitored using the microscope on the mask aligner with a 50x objective. The sample was removed from the TMAH after a period of 5 minutes, and the array was examined through the oxide squares to see how far the etchant had progressed. The oxide caps could then be judged as to when they would fall off by the size of the tip seen. The sample was placed back in the etchant for 30 seconds, and examined again under the microscope to see if the caps had fallen off. If they had, the sample was stripped of the remaining oxide, rinsed, and blown dry. If not, the above procedure was repeated. Figure 28 depicts the etching sequence of the nano-tip array.

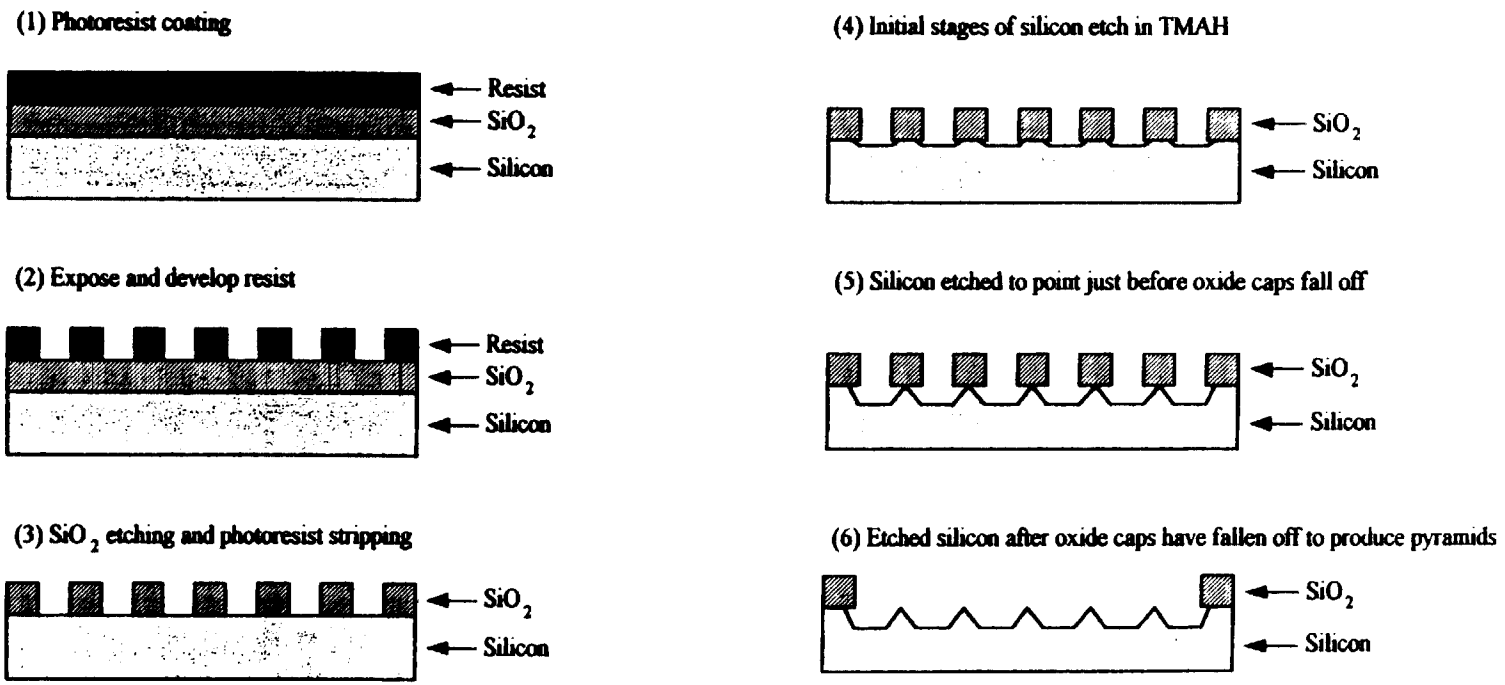

Figure 27. Schematic representation of nano-tip array fabrication.

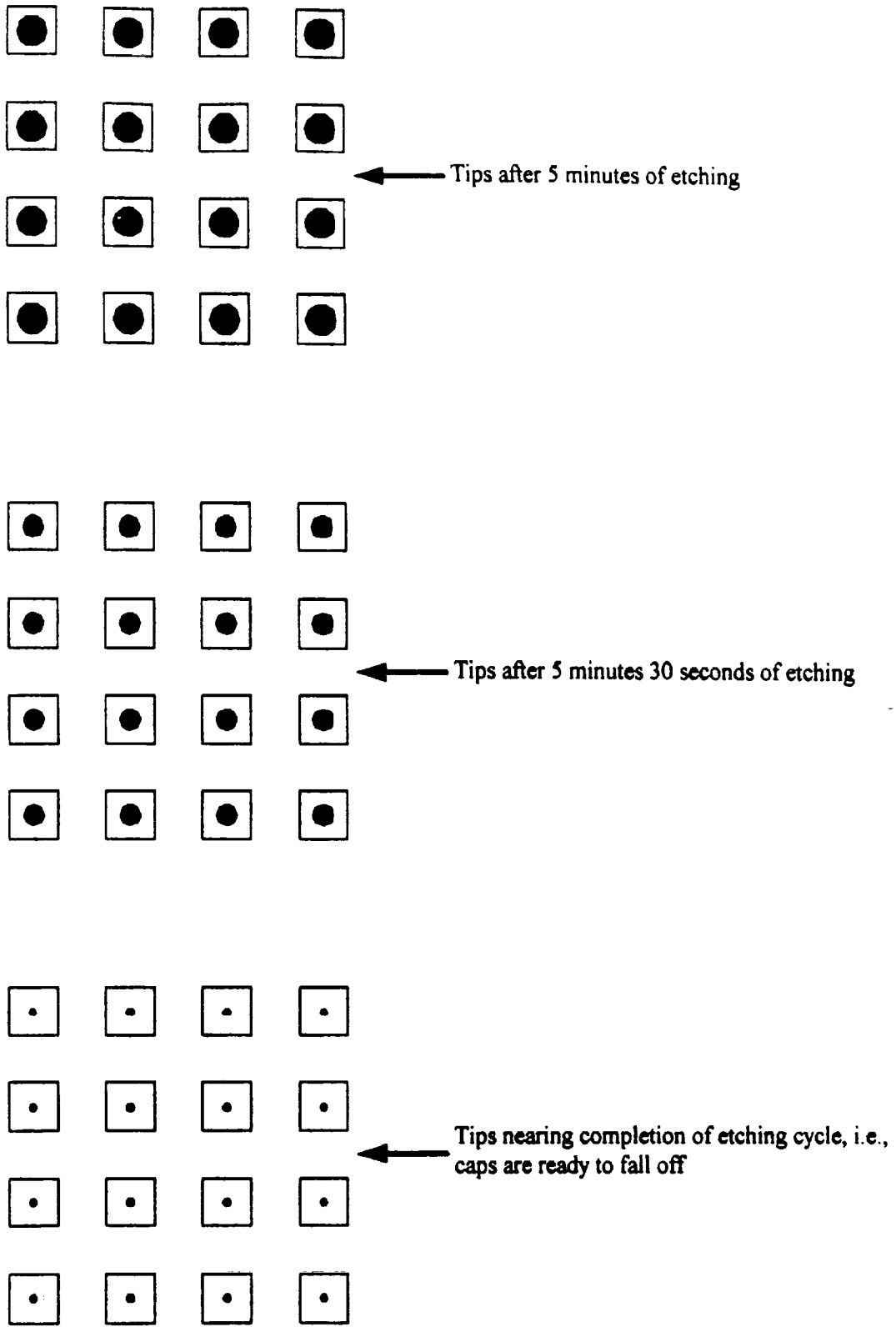

Figure 28. Etching sequence of nano-tip array.

The next step in the fabrication of the nano-tip array was to sharpen the tips. Research has shown that when sharp tips are created, the electric field is enhanced thereby lowering the voltage required for electron emission [40, 50, 87]. Hence, the tips of the array should be as sharp as possible. Sharpening of the tips was accomplished through thermal oxidation. During the oxidation process, oxygen reacts with the silicon surface to produce silicon dioxide (SiO_2), as previously discussed, thus silicon is consumed. The silicon that is consumed is from the sides of the nano-tips, and therefore, the tips are sharpened. Research has shown that maximum sharpness is achieved with a 1 hour oxidation [76]. The 1 hour oxidation also serves as a spacer when the nano-tip array and diaphragm are bonded. After oxidation, a mask was used to preserve the oxide around the edges of the array, and the oxide was removed from the array itself. Figures 29 and 30 are examples of a typical array and nano-tip.

3.2.2 Diaphragm

The diaphragm is the simplest of the two structures to fabricate. A sample was cleaned using H_2SO_4-H_2O_2 solution and ultrasonic agitation. The sample was then oxidized for a period of 135 minutes; this provided an oxide ~ 0.7 μm thick. As explained, SiO_2 acts as a mask to protect silicon from being etched by TMAH. Oxide is etched by the etchant, however, at a very slow rate (~124 A/hr). The thickness needed for the diaphragm requires it to remain in the TMAH for hours rather than minutes, as in the case of the array, so a thicker oxide is needed. The mask used for the diaphragm is comprised of a 4 mm x 4 mm square opening in a black field background. Photoresist was spun on the sample, the mask was placed in contact with the substrate and was exposed with ultraviolet light. The photoresist was developed, the underlying oxide

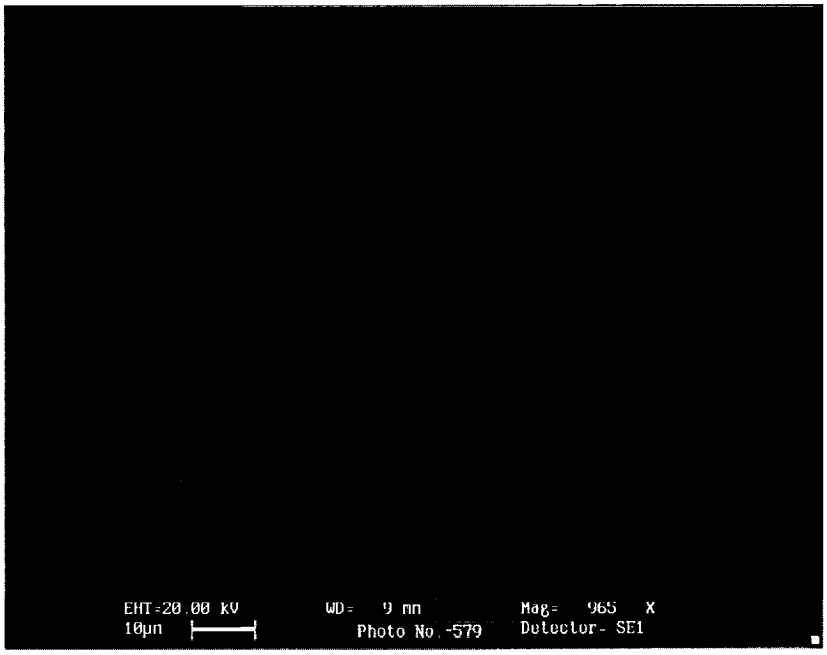

Figure 29. Typical silicon nano-tip array.

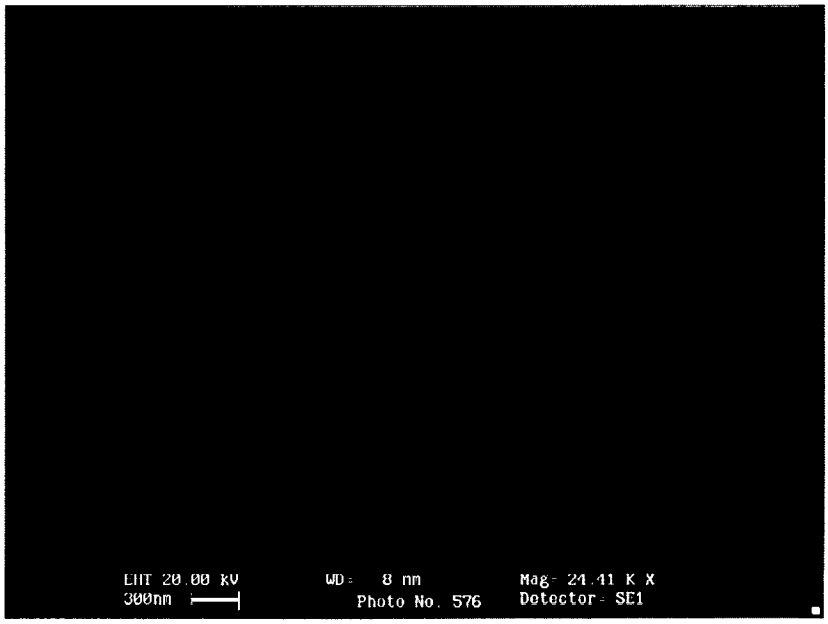

Figure 30. Silicon nano-tip at high magnification.

was removed, and the exposed silicon was etched in a concentration of 25% TMAH at 95 °C for ~3.5 hours. The protecting layer of oxide was removed and re-oxidation of the sample for a period of 4 hours was accomplished; this 1 μm oxide along with the 0.5 μm oxide grown around the edges of the nano-tip array provide the spacer needed for proper device operation when the two structures are bonded. Figure 31 shows a cross-section of a diaphragm that was used in an experiment to aid in determining diaphragm thickness.

3.2.3 Diamond Growth

Diamond growth is achieved on the nano-tip array using a Microwave Plasma-Enhanced Chemical Vapor Depositon (MPCVD) system, which involves striking a plasma consisting of hydrogen and methane. A diagram of the MPCVD system is shown in Figure 32. This system consists of a main vacuum chamber, mechanical and turbo-molecular pumps, an adjustable substrate holder with heater, gas inlet lines, a microwave source, and waveguide.

After pre-treatment of the nano-tip array, which involves creating nucleation sites for diamond [54], it was placed onto the substrate holder inside the main chamber. The chamber was pumped down and the gases conducive to diamond growth, hydrogen and methane, were allowed to enter the chamber using mass flow controllers to vary the gas mixture concentration. The throttle valve was used to bring the pressure up to ~ 20 Torr, the substrate was heated to 600 °C, and the microwave source was turned on. The waveguide directs the microwaves down onto the gas mixture in order to strike a plasma. Once the gases were ignited, the substrate holder was moved up until the substrate containing the array was sitting directly under the plasma ball. A negative bias was applied to enhance the nucleation [88, 89]. As the growth proceeds, the carbon atoms in

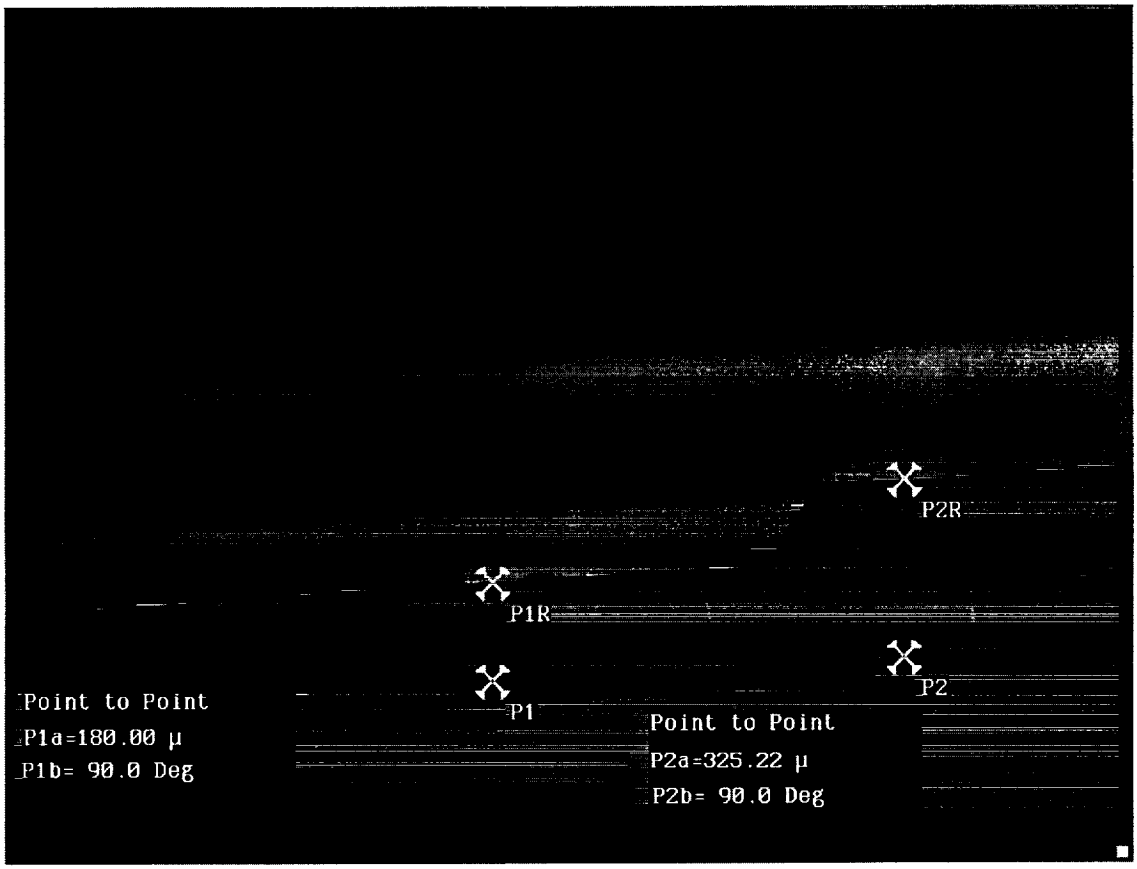

Figure 31. Cross-section of typical diaphragm: X's show thickness of diaphragm.

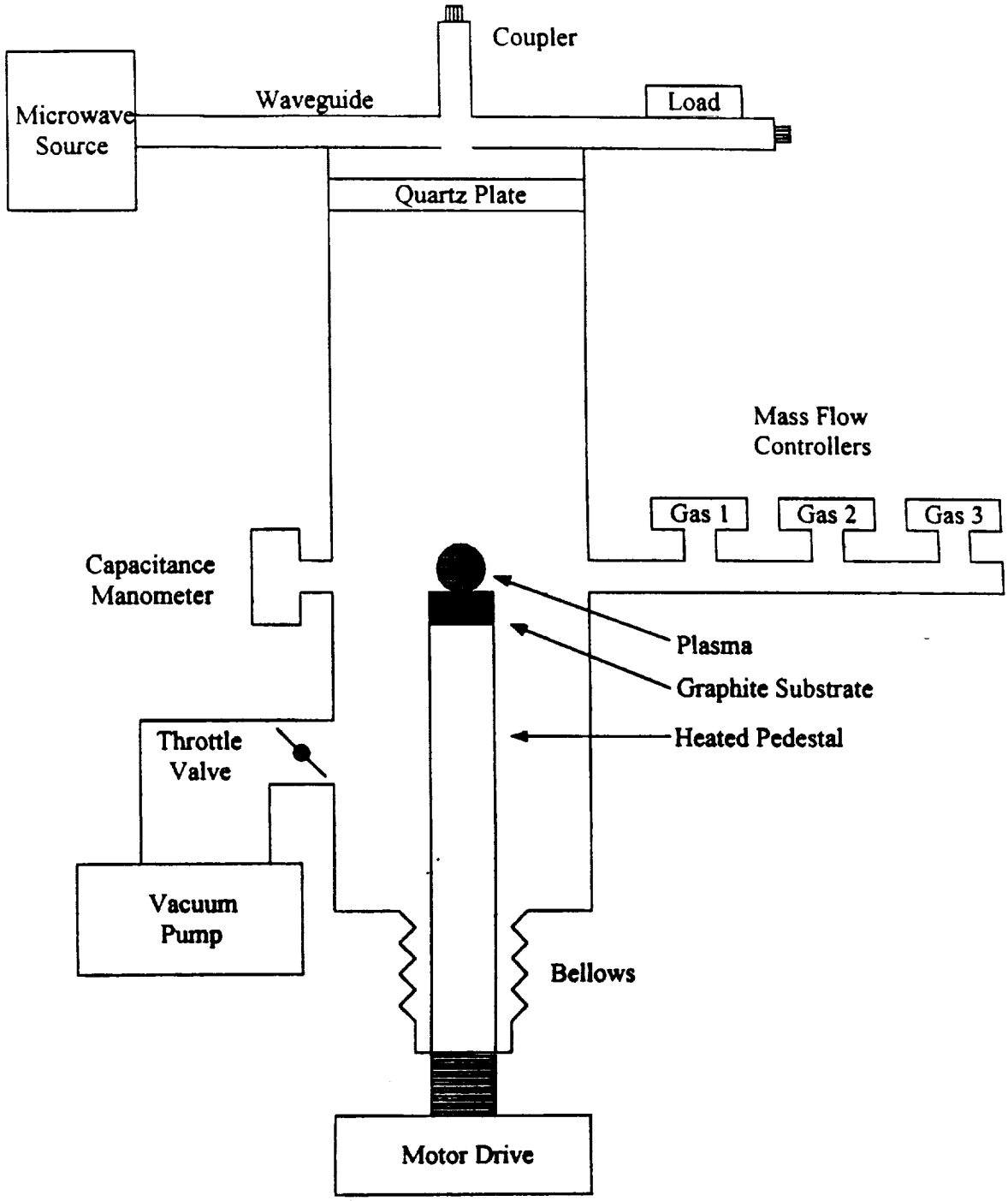

Figure 32. Microwave Plasma Chemical Vapor Deposition (MPCVD) System.

the plasma come into contact with the nucleation sites and diamond is formed. [90]. After plasma ignition, the pressure was increased to 35 Torr. The concentration of methane to hydrogen used was 2%, and growth proceeded for 30 minutes. A bias of -150 V was applied to the substrate for a period of 15 minutes at the beginning of growth. Figure 33 shows an example of a typical array after diamond growth.

3.2.4 Bonding

In the early stages of research, the nano-tip array and the diaphragm were bonded using epoxy. The structures were placed in contact with each other and epoxy was applied around the edge of the newly formed transducer. This method, while simple, had a few problems. Although the samples looked to be in contact when the epoxy was applied, it could not be determined if the epoxy had gotten in between the sandwich causing the spacing between the diaphragm and the array to increase. This spacing is crucial for correct operation. Other methods of bonding are being attempted and are discussed in Chapter 5.

3.3 Testing

After bonding, a contact was placed on either side of the pressure sensor using conductive epoxy, and the device was placed inside a pressure chamber. The pressure chamber was placed inside a temperature controlled structure to monitor the effect of temperature on the device. Voltages between 0 and 5 volts and pressures ranging from 1.013×10^5 to 2.392×10^5 Pa were applied to the sensor, and the output voltage across a 100k ohm resistor placed in series with the sensor was measured. Figure 34 shows a diagram of the test setup used for measurement. All testing was conducted at NASA Langley Research Center.

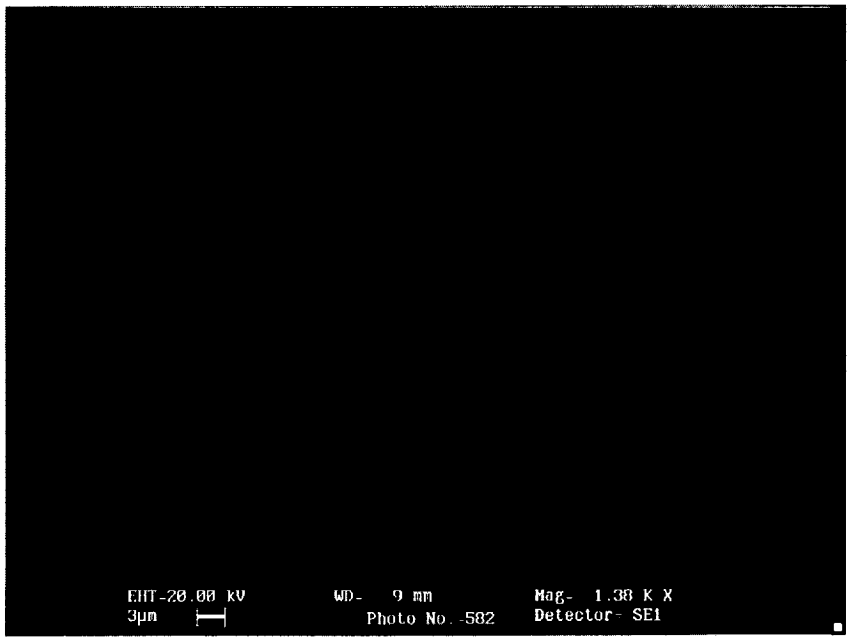

Figure 33. Typical diamond-coated array.

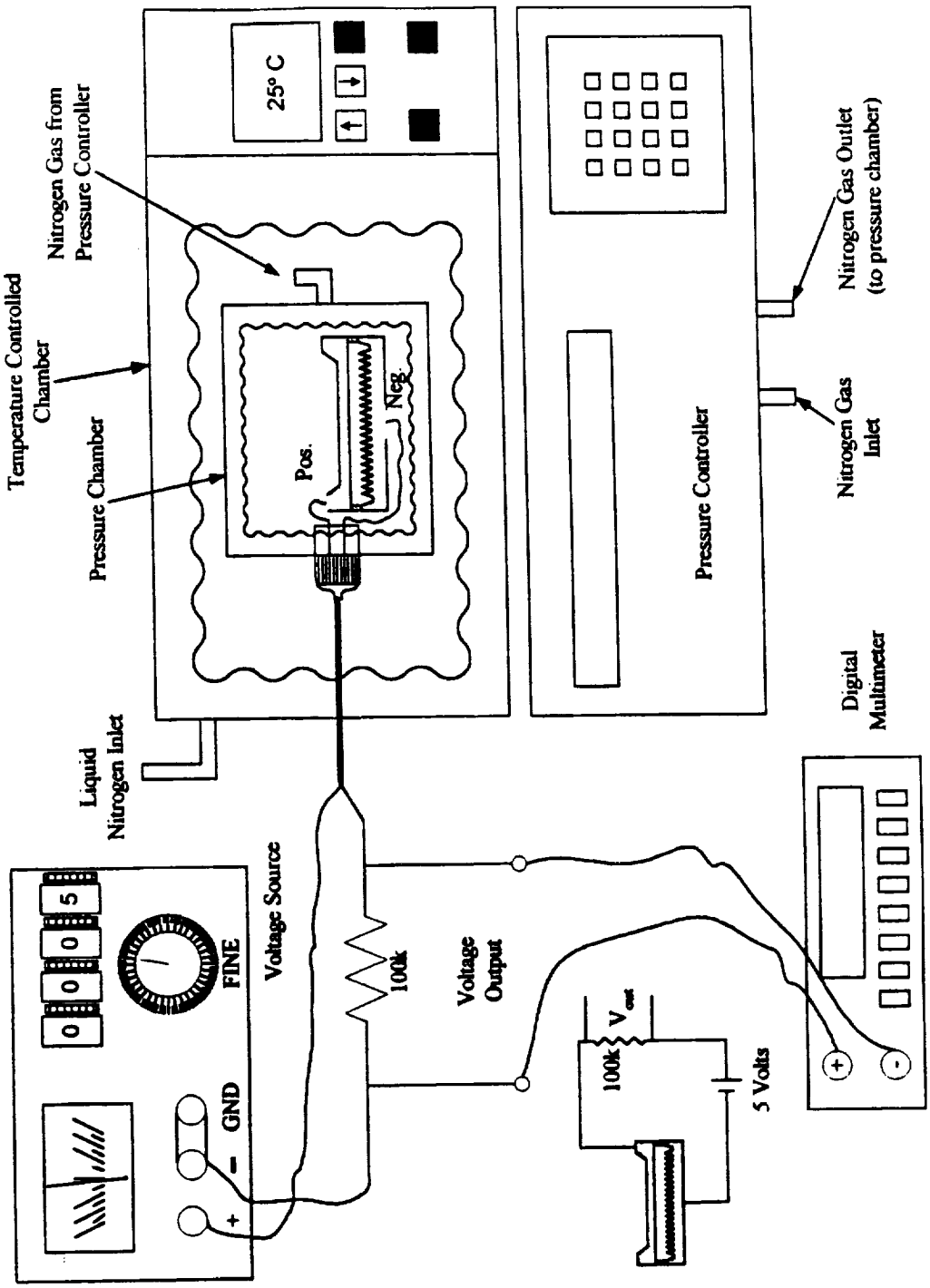

Figure 34. Test setup used for pressure sensor.

IV. RESULTS AND DISCUSSION

Eight sets of nano-tip arrays and diaphragms were fabricated and bonded using epoxy. In this section the results obtained from the fabrication process and subsequent testing are discussed.

4.1 Field Emitter Array and Diaphragm

The field emitter arrays were fabricated under identical conditions using the procedure described in Section 3. Figure 35 shows a scanning electron microscope (SEM) image of a diamond coated array. The array consists of 400 nano-tips arranged in a 20 x 20 configuration. The height and the radii of the tips are ~ 2 μm and ~ 50 nm, respectively. An SEM of a diamond coated tip is shown in Figure 36. The diamond film grown is ~100 nm thick and, as can be seen from the figure, conforms to the nano-tip of the array.

Two sets of diaphragms have been made: ~135 μm for sealing at atmospheric pressure and ~175 μm for sealing in vacuum. The diaphragm thickness was measured by calibrating an eyepiece with cross-hairs and a 50x microscope objective to the (111) plane exposed during the etch cycle. The thickness of the silicon sample is measured using a micrometer before processing. Using the objective and eyepiece, the amount of silicon that has been etched away is determined and subtracted from the initial value. This method allows for the control and uniformity of thicknesses from one diaphragm to another.

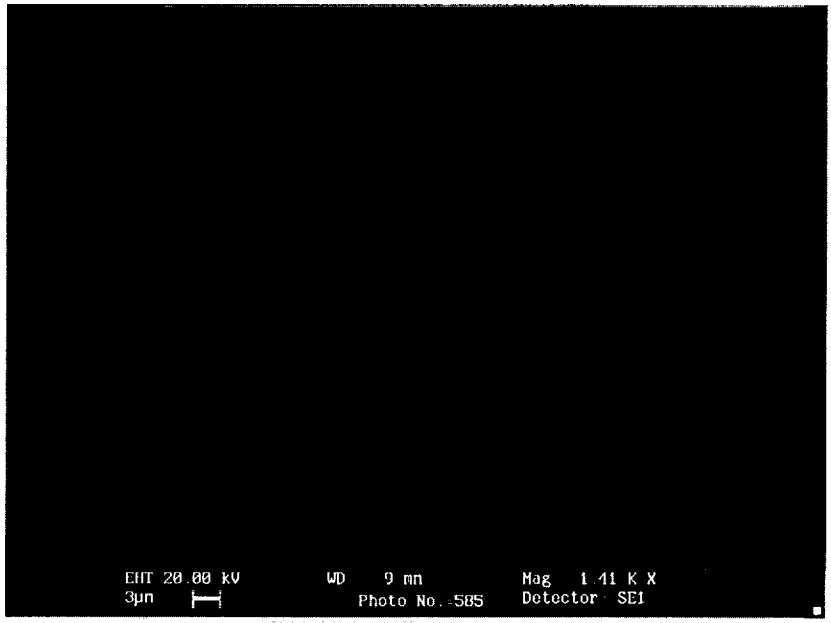

Figure 35. Diamond coated FEA.

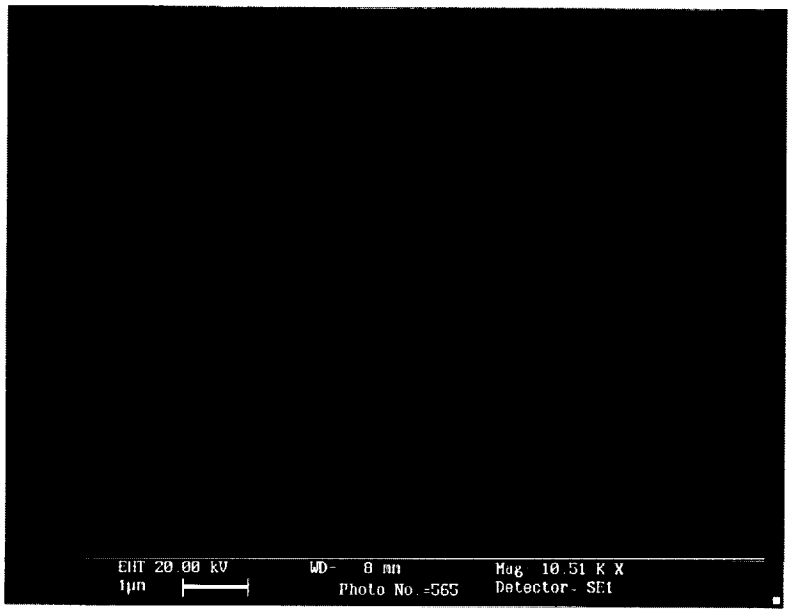

Figure 36. Diamond coated nano-tip.

4.3 Pressure Transducer Characteristics

The first four pressure sensors were made by placing the diaphragm on top of the nano-tip array in an air medium and sealing around the edges with epoxy, as explained in Chapter 3. During testing, large fluctuations in the output voltage were observed, and as such, no useable data could be obtained. It was determined that the most likely cause of the fluctuations was a discharge effect due to the ionization of air inside the devices.

For discharge to occur, the applied field should reach the ionization potential of at least one of the gases that comprise air, of which oxygen has the lowest at 12.063 eV [3]. The minimum free path for ionization is given by [91]:

$$\lambda_i = \frac{V_i}{E} \tag{64}$$

where V_i is the ionization potential of the gas and E is the electric field determined by the voltage applied to the nano-tip array multiplied by the field conversion factor, β. The field conversion factor calculated using Equation 54 has a minimum value of 2.933×10^7 cm^{-1} when the diaphragm is not deflected. Using the ionization potential of oxygen and an applied voltage of 5 volts, the minimum mean free path that an electron has to travel to cause ionization is 82.2 nm.

Another parameter that is important when considering discharge effects is the mean free path of the gas, λ_g, i.e., the spacing between the gas molecules. This is given by [91]:

$$\lambda_g = \frac{kT}{p\pi\sigma^2\sqrt{2}} \tag{65}$$

where k is Boltzmann's constant, T is temperature, p is pressure, and σ is the diameter of the gas molecule. For air, with an approximate diameter of 13.65 A [92], λ_g is 658.4 nm at standard temperature and pressure.

The mean free path of air along with the minimum free path that an electron needs to travel to gain enough energy to cause ionization are within the design parameters of the pressure sensor, i.e. the spacing (1.5 μm) between the diaphragm and the nano-tip array facilitate the ionization of oxygen hence, it is most likely occurring.

The ideal solution to combat the discharge effect would be to seal the device in vacuum; methods by which to bond the device in vacuum are being researched. In the interim, helium was used as the medium in which the two structures, the diaphragm and the array, were sealed. Helium has the highest ionization potential [3], 24.481 eV, thus, the mean free path that an electron requires to cause ionization is 113.1 nm, which is much higher than that of oxygen. Also, the diameter of helium is 0.62 A, which makes the mean free path of helium 319.1 μm at STP. Thus, the discharge effects will be minimized.

Figures 37 and 38 show graphs of the output voltage across the 100k ohm resistor vs. pressure for applied voltages of 1 and 5 volts, respectively, and pressures from 0 to 1.379×10^5 Pa with 1.013×10^5 Pa being the reference pressure. The effects of various temperatures are also shown. The input voltage was limited to 5 volts as these sensors are to be incorporated into digital circuits. Applied voltages of 2, 3, and 4 volts followed the same trend as seen in Figures 37 and 38, the only difference being an increase in the output voltages. As the applied voltage was incremented at a specific temperature, the output voltage also increased, as is shown in Figure 39.

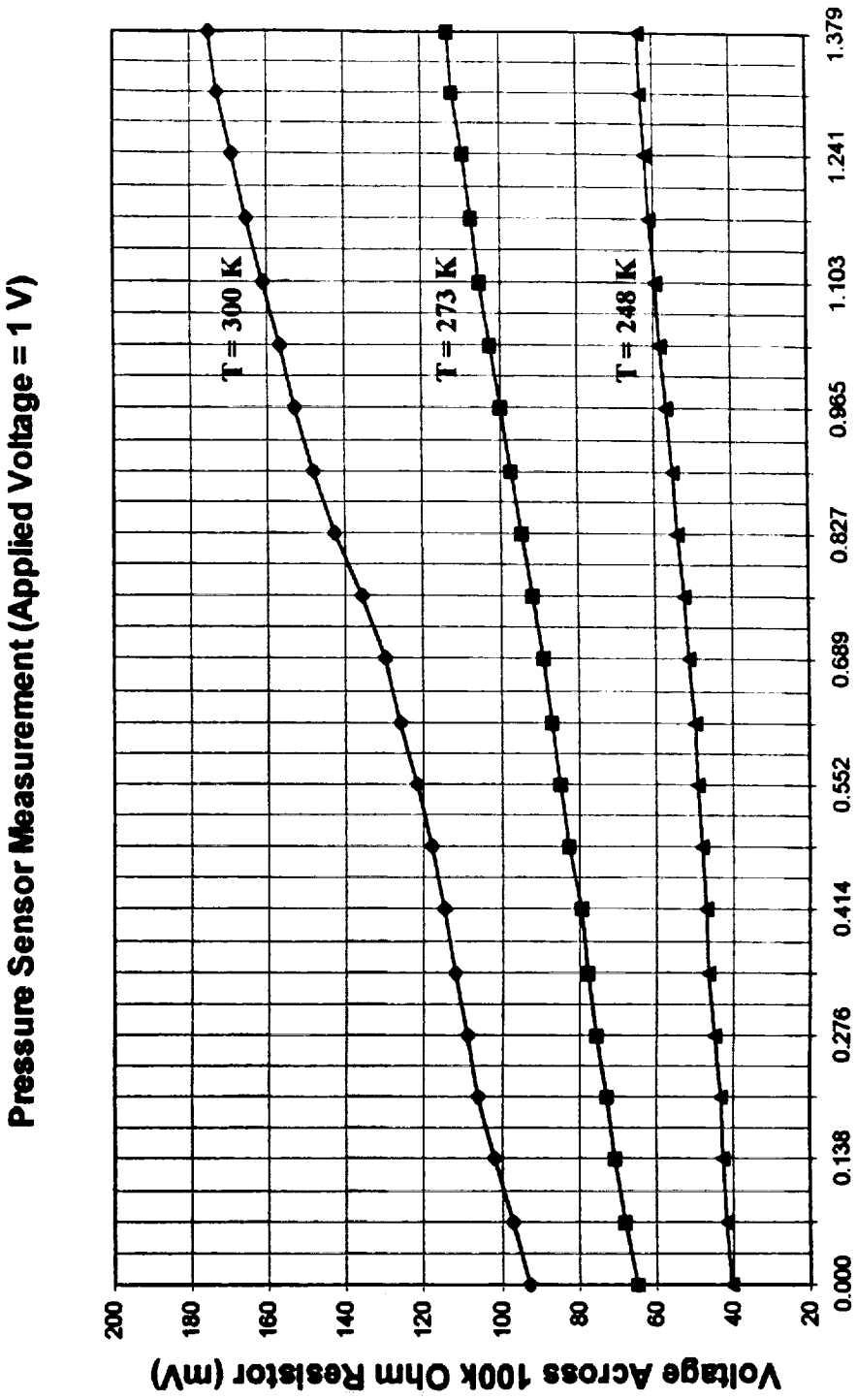

Figure 37. Voltage vs. Pressure Graph for applied voltage of 1 Volt.

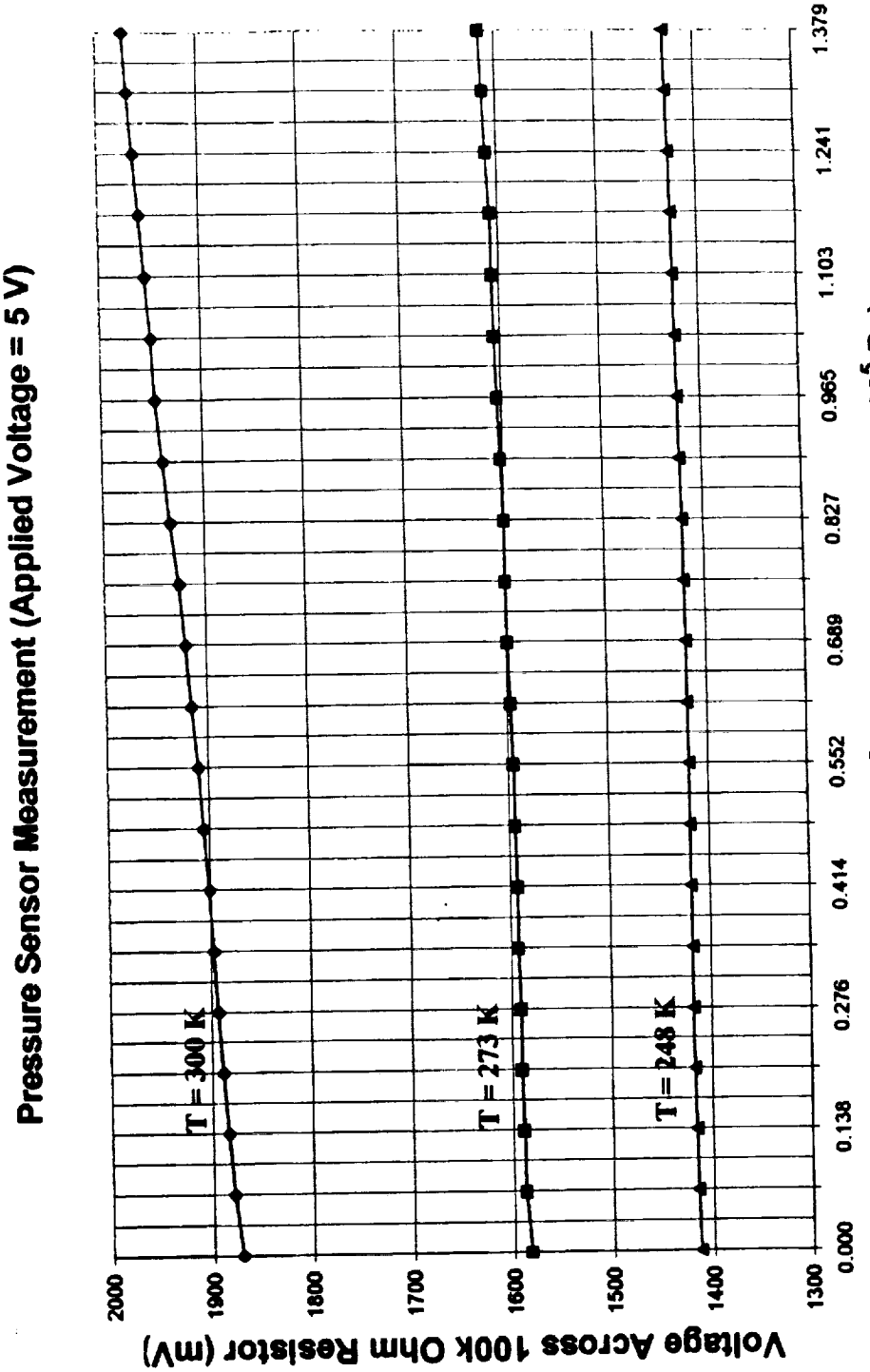

Figure 38. Voltage vs. Pressure graph for applied voltage of 5 Volts.

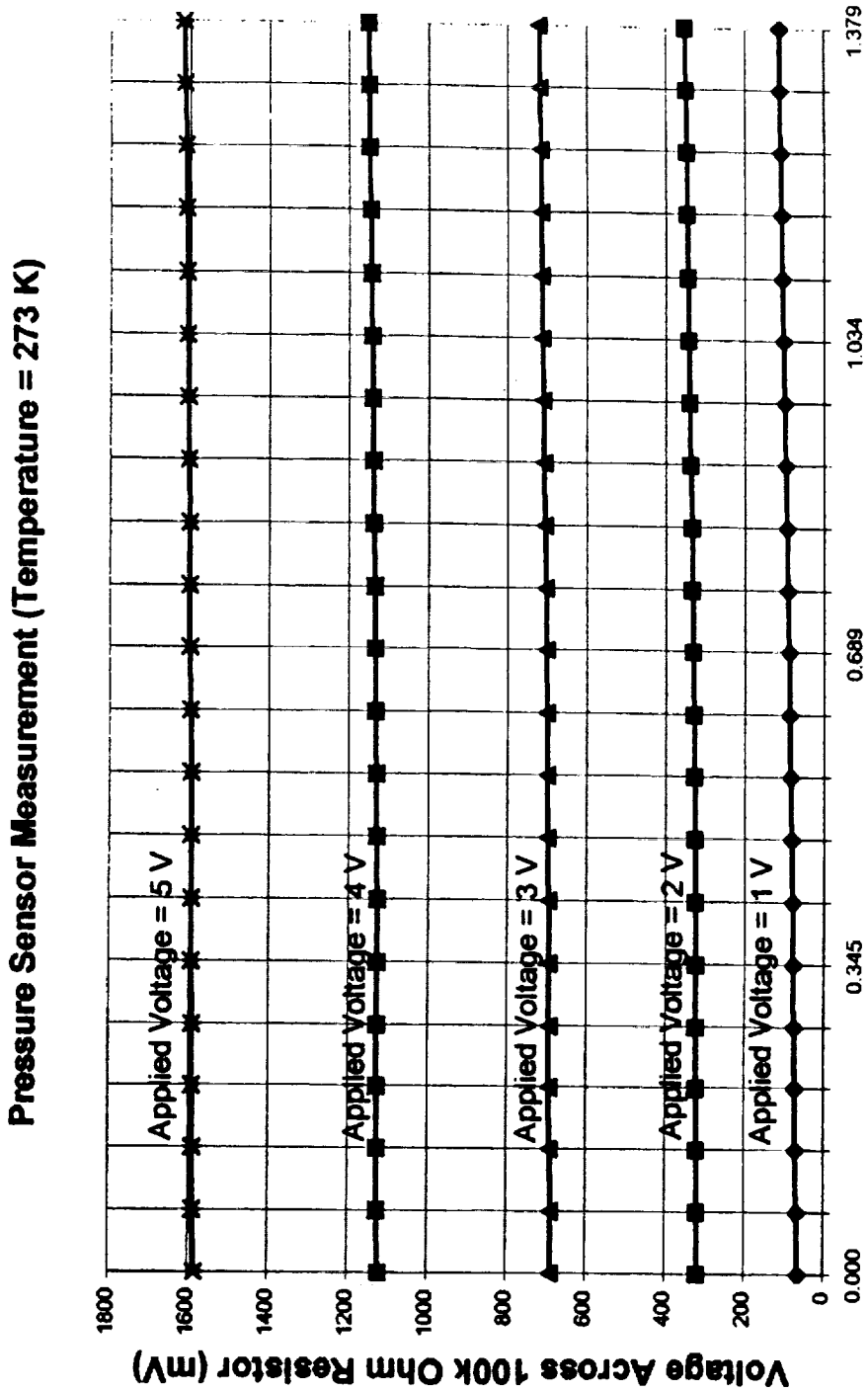

Figure 39. Voltage vs. Pressure graph at constant temperature.

4.4 Discussion

The theoretical graph of Figure 17 indicates that as the gap between the nano-tip array and diaphragm becomes smaller, current will increase exponentially as a result of the F-N equation for field emission. Since current is directly proportional to voltage and the deflection of the diaphragm is directly proportional to the pressure applied, the voltage obtained across the 100k ohm resistor should follow an exponential curve as well. Furthermore, if the voltage is plotted on a logarithmic scale while the pressure is plotted on a linear scale, a straight line should result. Figures 40 and 41 show the data plotted using semi-log graphs. The data in these figures is linear as is expected, however, the operating region depicted in Figure 15 was not achieved. Instead, operation is occurring for a larger tip array - diaphragm separation.

The unexpected behavior requiring explanation is that of temperature dependence in the output voltage. As the temperature was decreased, the output voltage also decreased. The Fowler-Nordheim equation for field emission is independent of temperature. One possible explanation for the temperature dependence may be due to the type and doping of the semiconductor used. The pressure sensor used to obtain the results was constructed from n-type silicon doped with phosphorus. The dopant concentration was determined from the resistivity to be on the order of 10^{15} cm^{-3} [41]. Field emission in n-type semiconductors is mainly from the conduction band, and the electrons in the conduction band come mainly from the ionization of the dopant atoms. When the temperature is decreased, the number of ionized donors is decreased leading to fewer electrons available for field emission. One of the models of emission from diamond has hypothesized that since diamond has a negative electron affinity (NEA), all

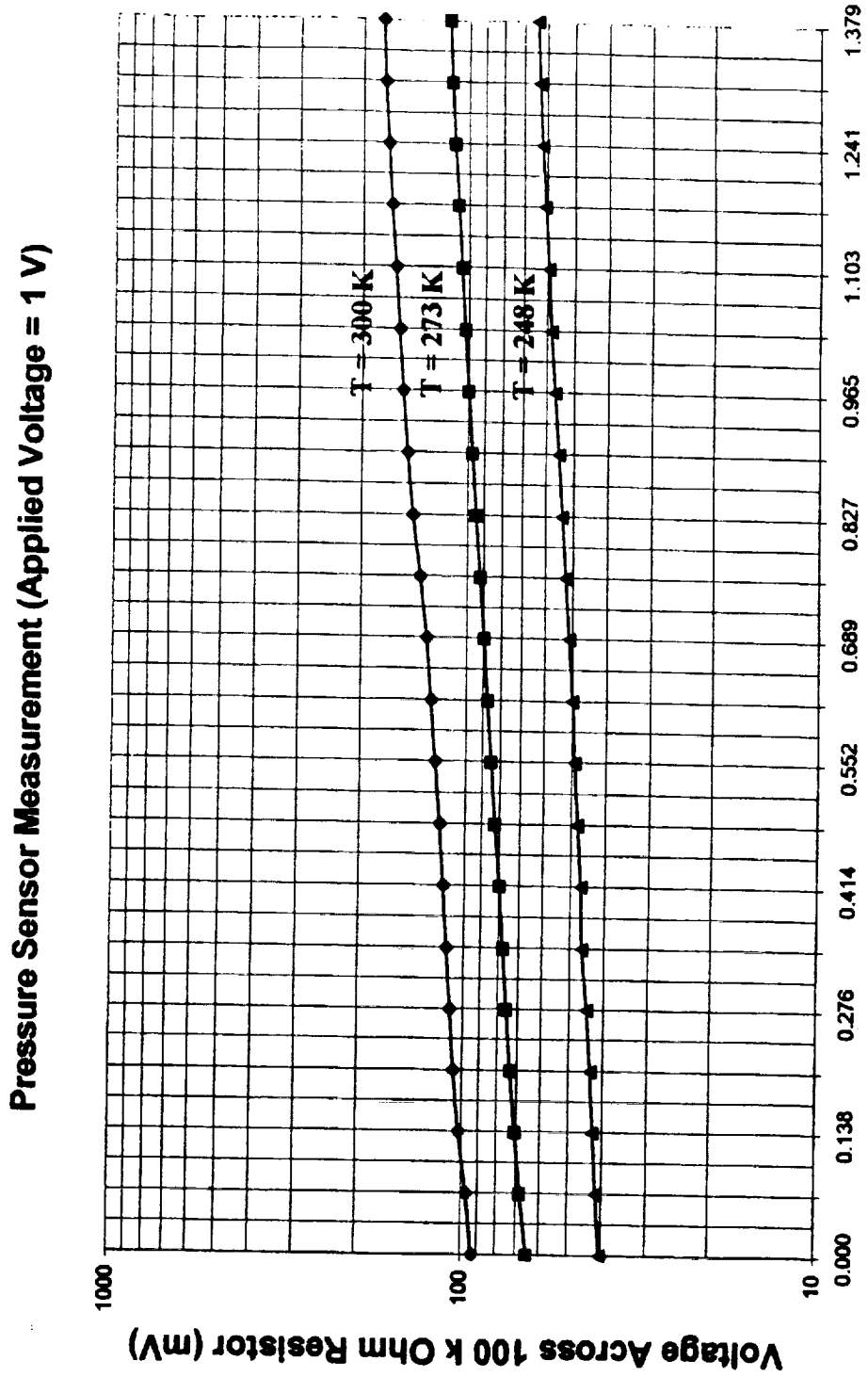

Figure 40. Semi-log plot of Voltage vs. Pressure for applied voltage of 1 Volt.

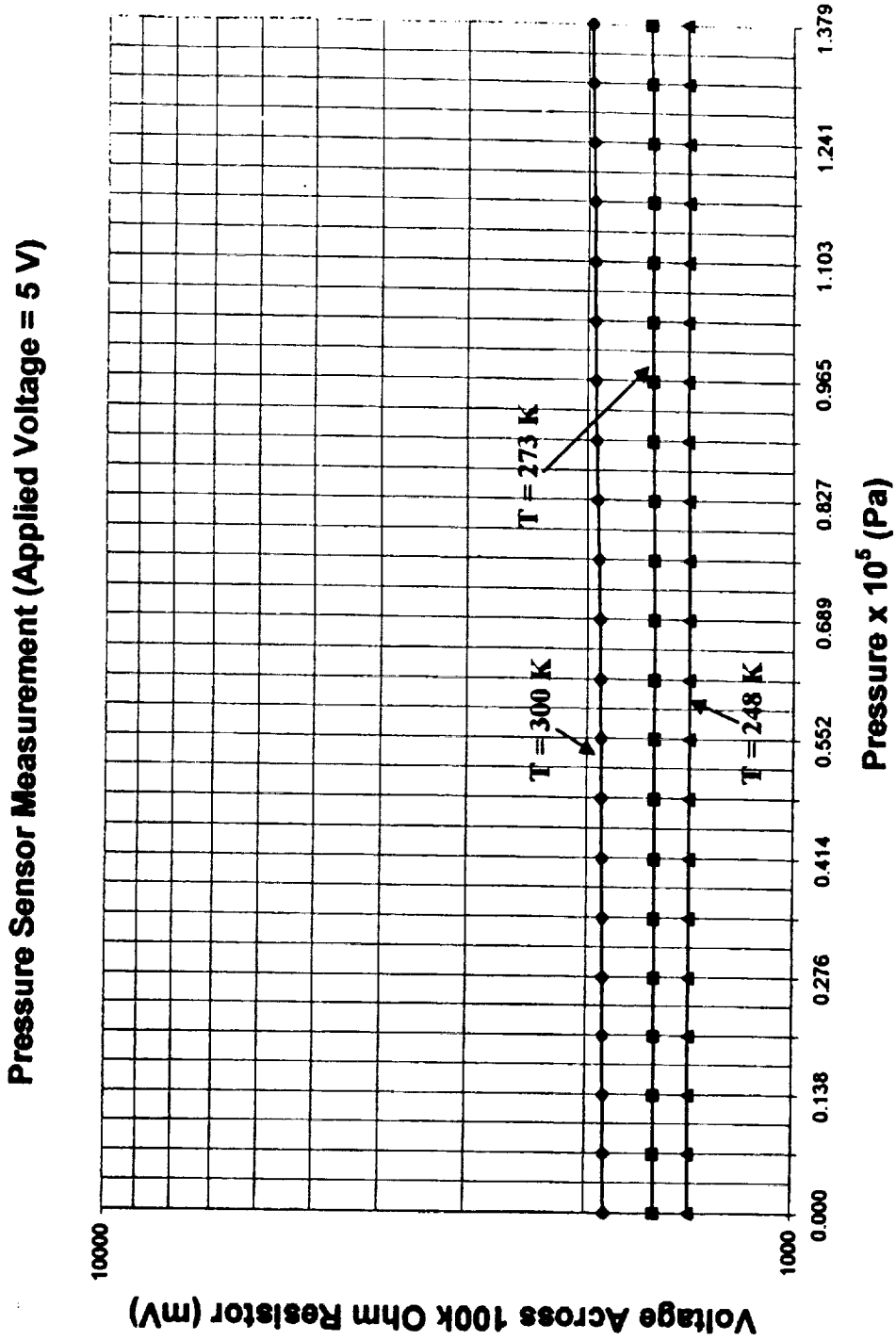

Figure 41. Semi-log plot of Voltage vs. Pressure for applied voltage of 5 Volts.

that is required for emission is to tunnel electrons from the semiconductor to the conduction band of diamond.

Sensitivity for pressure sensors is defined as:

$$Sensitivity = \frac{V_{max} - V_{min}}{P_{max} - P_{min}} x \frac{1}{V_{applied}} \qquad (66)$$

where (V_{max} - V_{min}) is the difference in output voltage at the extrema of applied pressures. The units of sensitivity are millivolts per volt per pound per square inch (mV/V/psi). Table 4 lists the sensitivity of the transducer for the various applied voltages and temperatures.

Table 4. Transducer Sensitivity

Applied Voltage (V)	Temperature (K)	V_{max} (mV)	V_{min} (mV)	$(P_{max} - P_{min})$ (psi)	Sensitivity (mV/V/psi)
1	248	63.9	40.4	20	1.18
	273	113.5	65		2.42
	300	175.4	93		4.12
2	248	273	255	20	0.45
	273	352	319		0.825
	300	506	407		2.48
3	248	605	588	20	0.283
	273	721	687		0.567
	300	948	843		1.75
4	248	1000	981	20	0.238
	273	1151	1121		0.375
	300	1444	1341		1.29
5	248	1430	1413	20	0.17
	273	1616	1583		0.33
	300	1974	1871		1.03

V. CONCLUSIONS

A new type of pressure sensor has been fabricated through the micro-machining of silicon. It consists of two structures: a diamond coated nano-tip array and a diaphragm. The processes used to form each structure have been discussed. The array consists of 400 tips arranged in a 20 x 20 configuration. Although the region of operation of the sensor is lower on the exponential curve than expected, the average sensitivity was found to be 2.13 millivolts per volt per psi over the range of applied voltages, which is comparable to piezo-resistive and capacitive pressure sensors using silicon diaphragms fabricated in a similar manner to the ones used here [22, 29, 30]. The structures bonded in air at atmospheric pressure exhibited discharge effects due to ionization; this effect was minimized by sealing the devices in helium. Temperature dependence of the sensors was noted.

5.1 Future Research

The results presented here show promise for devices fabricated using field emission. Additional research and modifications are underway to improve the sensor characteristics. The main issues under investigation are the bonding of the two structures (array and diaphragm), the temperature dependence, and sensitivity of the sensor.

5.1.1 Temperature Dependence

Research on the temperature dependence of field emission from diamond films has found that depositing boron doped p-type diamond eliminates the temperature

dependence [93, 94]. Samples have been fabricated with p-type diamond films grown on the nano-tip array. They will be tested after bonding in vacuum.

5.1.2 Sensitivity

The sensitivity of this sensor is comparable to those that have been fabricated by other means, but improvements are necessary. Sensitivity can be improved by using thinner diaphragms. The pressure range may decrease as a consequence, but precision will be gained. It is suspected that bonding with epoxy may play a role as to why the behavior was such as to be low on the operating curve. Alternative methods of bonding are being explored to eliminate this problem.

5.1.3 Bonding

Bonding with epoxy has several problems. The epoxy may get in between the two structures causing a larger gap than is required for proper operation. Pin holes in the epoxy could allow the helium gas to leak out of the device, thereby reverting back to the original configuration that showed discharge effects. When the devices are sealed, the epoxy may be out gassing into the sensor as it is drying, and this may also cause problems. Rather than try and compensate for these effects, the elimination of epoxy from the bonding scheme has been considered; this requires an alternative method of bonding. Two methods are being investigated: anodic bonding [95-98] and direct bonding [99-109] of the structures.

Anodic bonding is a process whereby silicon is placed in contact with a special type of glass that contains sodium ions. The contacted silicon and glass are then heated and an electric field is applied between them such that the sodium ions interact with the

silicon and form a bond. Experimentation is in progress to conduct anodic bonding for the pressure sensor. This method requires that the nano-tip array and diaphragm be fabricated on the same silicon substrate with the array on one side, as shown in Figure 42.

Direct bonding is also under study. This method can be used to bond silicon to silicon, silicon dioxide to silicon dioxide, and silicon dioxide to silicon. Direct bonding is the primary method used to create silicon on insulator devices, with device processing taking place after the bonding. Extending this technology to bond wafers with structures fabricated prior to bonding is being explored. Direct bonding involves placing two silicon wafers in contact with each other at low temperatures to form weak bonds and then annealing them at elevated temperatures to strengthen the bonds. Bonding of two oxidized silicon wafers has been accomplished at Old Dominion University, and experiments are in progress to facilitate the bonding of the array and diaphragm. Two-inch wafers have been processed. Each wafer contains either 16 arrays or 16 diaphragms arranged in a 4 x 4 configuration. The direct bonding method is the most promising as it will provide sensors completely made out of silicon.

5.2 Applications

The main application of this type of pressure sensor is to detect pressure changes in the air flow across the wings of aircraft. When an aircraft moves through the air, the flow across the wings can be laminar or turbulent. When it is turbulent, more fuel is consumed than when it is laminar. Pressure changes accompany the transition from laminar flow to turbulent flow. If the pressure can be sensed when this occurs, the structure of the wing can then be slightly modified so that laminar flow is kept constant, thereby conserving fuel. The temperature independent pressure sensor would eliminate

the need for temperature-correcting circuitry required of other pressure sensors, thereby reducing the overall weight and price of the aircraft. Other uses of this sensor include industrial, biomedical, and automobile instrumentation.

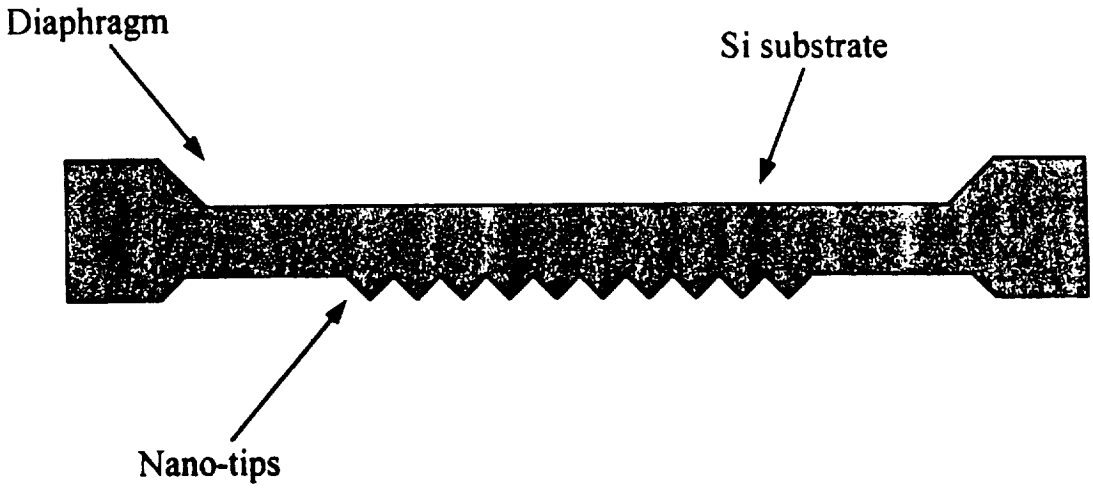

Figure 42. Nano-tip array and diaphragm on same substrate.

REFERENCES

[1] Benedict, Robert P., Fundamentals of Temperature, Pressure, and Flow Measurements, New York: John Wiley & Sons, Inc., 1977, pp. 287-337.

[2] Young, Hugh D., University Physics, Extended Version with Modern Physics, Massachusetts: Addison-Wesley Publishing Company, Inc., 1992, Appendix E.

[3] CRC Handbook of Chemistry and Physics, Weast, R. C., ed., Astle, M. J., Assoc. ed., Florida: CRC Press, Inc., 1978, pp. F-313 - F-335.

[4] Diels, K., Jaeckel, R.; Translated by Adam, H., Edwards, J., Leybold Vacuum Handbook, Oxford: Pergamon Press Ltd., 1966, pp. 100-118.

[5] Roberts, Richard W., Vanderslice, Thomas A., Ultrahigh Vacuum and its Applications, New Jersey: Prentice-Hall, Inc., 1963, pp. 30-58.

[6] Methods of Experimental Physics, Volume 14, Vacuum Physics and Technology, Weissler, G. L., ed., Carlson, R. W., ed., New York: Academic Press, Inc., 1979, pp. 35-80.

[7] Delchar, T. A., Vacuum Physics and Techniques, London: Chapman & Hall, 1993, pp. 110-152.

[8] Dushman, Saul, Scientific Foundations of Vacuum Technique, Lafferty, J. M., ed., New York: John Wiley & Sons, Inc., 1962, pp.220-353.

[9] Leck, J. H., Pressure Measurement In Vacuum Systems, London: Chapman & Hall Ltd., 1957, pp. 11-20, 103-124.

[10] Yarwood, J., High Vacuum Technique, Theory, Practice, Industrial Application and Properties of Materials, London: Chapman & Hall Ltd., 1956, pp. 73-107.

[11] Neubert, Hermann K. P., Instrument Transducers, An Introduction To Their Performance and Design, London: Oxford University Press, 1963, pp. 48-60.

[12] Norton, Harry N., Handbook of Transducers, New Jersey: Prentice-Hall, Inc., 1989, pp. 294-330.

[13] Norton, Harry N., Handbook of Tranducers for Electronic Measuring Systems, New Jersey: Prentice-Hall, Inc., 1969, pp. 418-464.

[14] Hordeski, Michael F., Transducers For Automation, New York: Van Nostrand Reinhold Company, Inc., 1987, pp. 50-69.

[15] Seippel, Robert G., Transducers, Sensors, & Detectors, Virginia: Reston Publishing Company, Inc., 1983, pp. 192-216.

[16] Lyons, Jerry L., The Designer's Handbook of Pressure-Sensing Devices, New York: Van Nostrand Reinhold Company, 1980, pp. 147-151.

[17] Neubert, Hermann K. P., Strain Gauges, Kinds and Uses, London: Macmillan & Co, Ltd., 1967, pp. 20, 137-144.

[18] Tohyama, O., Kohashi, M., Yamamoto, K., Itoh, H. "A Fiber-Optic Silicon Pressure Sensor For Ultra-Thin Catheters," *Sensors and Actuators A*, Vol. 54, 1996, pp. 622-625.

[19] Ikeda, K., Kuwayama, H., Kobayashi, T., Watanabe, T., Nishikawa, T., Yoshida, T., Harada, K., "Three-dimensional Micromachining of Silicon Pressure Sensor Integrating Resonant Strain Gauge on Diaphragm," *Sensors and Actuators*, Vol. A21-A23, 1990, pp. 1007-1010.

[20] Tong, L., Hsu, J. T., Ko, W. H., Ding, X., "The Analysis of Capacitive Pressure Sensors with Large Deflection," *Transducers '91. 1991 International Conference on Solid-State Sensors and Actuators*, IEEE, New York, pp. 185-187.

[21] Matsumoto, Y., Shoji, S., Esashi, W., "A Miniature Integrated Capacitive Pressure Sensor," *Extended Abstracts of the 22nd (1990 International) Conference on Solid State Devices and Materials*, Tokyo, Japan, 1990, pp. 701-704.

[22] Esashi, M., Sugiyama, S., Ikeda, K., Wang, Y., Miyashita, H., "Vacuum-Sealed Silicon Micromachined Pressure Sensors," *Proceedings of the IEEE*, Vol. 86, No. 8, 1998, pp. 1627-1639.

[23] Pons, P., Blasquez, G., Ratier, N., "Harmonic Response of Silicon Capacitive Pressure Sensor," *Sensors and Actuators A*, Vol. 25-27, 1991, pp. 301-305.

[24] Smith, Charles S., "Piezoresistance Effect in Germanium and Silicon," *Physical Review*, Vol. 94, No. 1, 1954, pp. 42-49.

[25] Adams, E. N., "Elastoresistance in p-Type Ge and Si," *Physical Review*, Vol. 96, No. 3, 1954, pp. 803-804.

[26] Morin, F. J., Geballe, T. H., Herring, C., "Temperature Dependence of the Piezoresistance of High-Purity Silicon and Germanium," *Physical Review*, Vol. 105, No. 2, 1957, pp. 525-539.

[27] Tufte, O. N., Stelzer, E. L., "Piezoresistive Properties of Silicon Diffused Layers," *Journal of Applied Physics*, Vol. 34, No. 2, 1963, pp. 313-318.

[28] Chang, C. C., Lieu, C. T., Hsich, M. K., "Study of the Fabrication of a Silicon Pressure Sensor," *International Journal of Electronics*, Vol. 82, No. 3, 1997, pp. 295-302.

[29] Borky, J. M., Wise, K. D., "Intergrated Signal Conditioning for Silicon Pressure Sensors," *IEEE Transactions on Electron Devices*, Vol. ED-26, No. 12, 1979, pp. 1906-1910.

[30] Bao, M., Wang, Y., "Analysis and Design of a Four-Terminal Silicon Pressure Sensor at the Centre of a Diaphragm," *Sensors and Actuators*, Vol. 12, 1987, pp. 49-56.

[31] Shimazoe, M. Matsuoka, Y., Yasukawa, A., Tanabe, M., "A Special Diaphragm Pressure Sensor With High Output and High Accuracy," *Sensors and Actuators*, Vol. 2, 1982, pp. 275-282.

[32] Chung, G. S., Kawahito, S., Ishida, M., Nakamura, T., "High-Resolution Pressure Sensors by Silicon Wafer Direct Bonding," *Electronics Letters*, Vol. 27, No. 12, 1991, pp. 1098-1100.

[33] French, P. J., Muro, H., Shinohara, T., Nojiri, H., Kaneko, H., "SOI Pressure Sensor," *Sensors and Actuators A*, Vol. 35, 1992, pp. 17-22.

[34] Young, T. L., Seo, H. D., Kawamura, A., Yamada, T., Matsumoto, Y., Ishida, M., Nakamura, T., "Compensation Method Of Offset And Its Temperature Drift In Silicon Piezoresistive Pressure Sensor Using Double Wheatstone-Bridge Configuration," *8th International Conference on Solid-State Sensors and Actuators and Eurosensors IX. Digest of Technical Papers (IEEE Cat. No. 95TH8173)*, Vol. 2, pp. 570-573.

[35] Matsuoka, Y., Yamamoto, Y., Tobita, T., Shimada, S., Yasukawa, A., "Design Method for Sensing Body of Differential Pressure Transmitter Using Silicon Diaphragm-Type Pressure Sensor," *IEEE Transactions on Instrumentation and Measurement*, Vol. 44, No. 3, 1995, pp. 791-794.

[36] Wu, Xian-Ping, "A New Pressure Sensor with Innercompensation for Nonlinearity and Protection to Overpressure," *Sensors and Actuators*, Vol. A21-A23, 1990, pp. 65-69.

[37] Suzuki, K., Ishihara, T., Hirata, M., Tanigawa, H., "Nonlinear Analyses on CMOS Integrated Silicon Pressure Sensor," *International Electron Devices Meeting Technical Digest (Cat. No. 85CH22525)*, IEEE, New York, 1985, pp. 137-140.

[38] Funded by NASA Grant No. NGT-1-52194.

[39] Private communication with Dr. Sacharia Albin, Associate Professor, Old Dominion University, Department of Electrical and Computer Engineering.

[40] Spindt, C. A., Brodie, I., Humphrey, L., Westerberg, E. R., "Physical Properties of Thin-Film Field Emission Cathodes With Molybdenum Cones," *Journal of Applied Physics*, Vol. 47, No. 12, 1976, pp. 5248-5263.

[41] Sze, S. M., Semiconductor Devices, Physics and Technology, New York: John Wiley & Sons, 1985, pp. 8-28, 144, 166-169.

[42] Kasap, S. O., Principles of Electrical Engineering Materials and Devices, Massachusetts: Irwin McGraw-Hill, 1997, pp. 158-162, 183-186, 281-287.

[43] Fowler, R. H., Nordheim, L. W., "Electron Emission in Intense Electric Fields," *Proceedings of the Royal Society, London*, Vol. A119, 1928, pp. 173-181.

[44] Nordheim, L. W., "The Effect of the Image Force on the Emission and Reflexion of Electrons by Metals," *Proceeding of the Royal Society, London*, Vol. 121, pp. 626-639.

[45] Burgess, R. E., Kroemer, H., "Corrected Values of Fowler-Nordheim Field Emission Functions v(y) and s(y)," *Physical Review*, Vol. 90, No. 4, 1953, p. 515.

[46] Murphy, E. L., Good, Jr., R. H., "Thermionic Emission, Field Emission, and the Transition Region," *Physical Review*, Vol. 102, No. 6, 1956, pp. 1464-1473.

[47] Gomer, Robert, Field Emission and Field Ionization, Number 9, Harvard Monographs in Applied Science, Massachusetts: Harvard University Press, 1961, pp. 1-31.

[48] Stratton, Robert, "Theory of Field Emission from Semiconductors," *Physical Review*, Vol. 125, No. 1, 1962, pp. 67-82.

[49] Iannazzo, S., "A Survey of the Present Status of Vacuum Microelectronics," *Solid-State Electronics*, Vol. 36, No. 3, 1993, pp. 301-320.

[50] Cui, Z., Tong, L., "Optimum Geometry and Space-Charge Effects in Vacuum Microelectronic Devices," *IEEE Transactions on Electron Devices*, Vol. 40, No. 2, 1993, pp. 448-452.

[51] Zhirnov, V. V., Givargizov, E. I., Plekhanov, P. S., "Field Emission from Silicon Spikes with Diamond Coatings," *Journal of Vacuum Science and Technology B*, Vol. 13, No. 2, 1995, pp. 418-421.

[52] Roark, Raymond J., Formulas for Stress and Strain, New York: McGraw-Hill, Inc., 1965, pp. 214-258.

[53] Gildenblat, G. Sh., Schmidt, P. E., "Diamond," in Handbook on Semiconductor Parameters, Volume 1, New Jersey: World Scientific, 1996, pp. 58-77.

[54] Cole, Charles Randall, Selective CVD Growth of Diamond Crystals on Tungsten, Virginia: Old Dominion University, 1997, p. 2, 13-14.

[55] Mackie, W. A., Plumlee, J. E., Bell, A. E., "Work Function Measurements of Diamond Film Surfaces," *Journal of Vacuum Science and Technology B*, Vol. 14, No. 3, 1996, pp. 2041-2045.

[56] Yuan, G., Jin, C. C., Zhang, B. L., Jiang, H., Zhou, T. M., Ning, Y. Q., Wang, Y. Z., Wang, W. B., Jin, Y. X., Ji, H., Gu, C. Z., "Influence of Silicon Tip Arrays on Effective Work Function of Diamond," *Journal of Vacuum Science and Technology B*, Vol. 16, No. 2, 1998, pp. 710-711.

[57] Zhirnov, V. V., Voronin, A. B., Givargizov, E. I., Meshcheryakova, A. L., "Emission Stability and High Current Performance of Diamond-Coated Si Emitters," *Journal of Vacuum Science and Technology B*, Vol. 14, No. 3, 1996, pp. 2034-2036.

[58] Ji, H., Jin, Z. S., Wang, J. Y., Lu, X. Y., Gu, C. Z., Liu, B. B., Jin, W. C., Gao, C. X., Yuan, G., Wang, W. B., "Field Emission Characteristics of Diamond Films with Different Surface Morphologies," *Journal of Vacuum Science and Technology B*, Vol. 17, No. 2, 1999, pp. 684-687.

[59] Zhirnov, V. V., Kuttel, O. M., Groning, O., Alimova, A. N., Detkov, P. Y., Belobrov, P. I., Maillard-Schaller, E., Schlapbach, L., "Characterization of Field Emission Cathodes with Different Forms of Diamond Coatings," *Journal of Vacuum Science and Technology B*, Vol. 17, No. 2, 1999, pp. 666-669.

[60] Park, M., McGregor, D. R., Bergman, L., Nemanich, J., Hren, J. J., Cuomo, J. J., Choi,W. B., Zhirov, V. V., "Raman Analysis and Field Emission Study of Ion Beam Etched Diamond Films," *Journal of Vacuum Science and Technology B*, Vol. 17, No. 2, 1999, pp. 700-704.

[61] Evtukh, A. A., Litovchenko, V. G., Klyui, N. I., Marchenko, R. I., Kudzinovski, S. Yu., "Properties of Plasma Enhanced Chemical Vapor Deposition Diamond-Like Carbon Films as Field Electron Emitters Prepared in Different Regimes," *Journal of Vacuum Science and Technology B*, Vol. 17, No. 2, 1999, pp. 679-683.

[62] Kwon, S. J., Shin, Y. H., Aslam, D. M., Lee, J. D., "Field Emission Properties of the Polycrystalline Diamond Film Prepared by Microwave-Assisted Plasma Chemical Vapor Deposition," *Journal of Vacuum Science and Technology B*, Vol. 16, No. 2, 1998, pp. 712-715.

[63] Pupeter, N., Gohl, A., Habermann, T., Mahner, E., Muller, G., Piel, H., Niedermann, Ph., Hanni, W., "Field Emission Measurements with μm Resolution on Chemical-Vapor-Deposited Polycrystalline Diamond Films," *Journal of Vacuum Science and Technology B*,

Vol. 14, No. 3, 1996, pp. 2056-2059.

[64] Geis, M. W., Twichell, J. C., Lyszczarz, T. M., "Diamond Emitters Fabrication and Theory," *Journal of Vacuum Science and Technology B*, Vol. 14, No. 3, 1996, pp. 2060-2067.

[65] Rangelow, I. W., Shi, F., hudek, P., Grabiec, P., Volland, B., Givargizov, E. I., Stepanove, A. N., Obolenskaya, L. N., Mashkova, E. S., Molchanov, V. A., "Micromachined Ultrasharp Silicon and Diamond-Coated Silicon Tip as a Stable Field-Emission Electron Source and a Scanning Probe Microscopy Sensor with Atomic Sharpness," *Journal of Vacuum Science and Technology B*, Vol. 16, No. 6, pp. 3185-3191.

[66] Zhou, D., Krauss, A. R., Qin, L. C., McCauley, T. G., Gruen, D. M., Corrigan, T. D., Chang, R. P. H., Gnaser, H., "Synthesis and Electron Field Emission of Nanocrystalline Diamond Thin Films Grown from N_2/CH_4 Microwave Plasmas," *Journal of Applied Physics*, Vol. 82, No. 9, 1997, pp. 4546-4550.

[67] Sugino, T., Kawasaki, S., Yokota, Y., Iwasaki, Y., Shirafuji, J., "Electron Emission Characteristics of Polycrystalline Diamond Films," *Journal of Vacuum Science and Technology B*, Vol. 16, No. 2, 1998, pp. 720-723.

[68] Kang, W. P., Davidson, J. L., Howell, M., Bhuva, B., Kinser, D. L., Kerns, D. V., Li, Q., Xu, J. F., "Micropatterned Polycrystalline Diamond Field Emitter Vacuum Diode Arrays," *Journal of Vacuum Science and Technology B*, Vol. 14, No. 3, 1996, pp. 2068-2071.

[69] Ding, M. Q., Myers, A. F., Choi, W. B., Vispute, R. D., Camphausen, S. M., Narayan, J., Cuomo, J. J., Hren, J. J., Bruley, J., "Field Emission From Amorphous Diamond Coated Mo Tip Emitters by Pulsed Laser Deposition," *Journal of Vacuum Science and Technology B*, Vol. 15, No. 4, 1997, pp. 840-844.

[70] Mearini, G. T., Krainsky, I. L., Dayton, Jr., J. A., Wang, Y., Sorman, C. A., Angus, J. C., Hoffman, R. W., Anderson, D. F., "Stable Secondary Electron Emission From Chemical Vapor Deposited Diamond Films Coated With Alkali-Halides," *Applied Physics Letters*, Vol. 66, No. 2, 1995, pp. 242-244.

[71] Zhu, W., Kochanski, G. P., Jin, S., Seibles, L., "Defect-Enhanced Electron Field Emission From Chemical Vapor Deposited Diamond," *Journal of Applied Physics*, Vol. 78, No. 4, 1995, pp.2707-2711.

[72] Ding, M. Q., Gruen, D. M., Krauss, A. R., Auciello, O., Corrigan, T. D., Chang, R. P. H., "Studies of Field Emission From Bias-Grown Diamond Thin Films," *Journal of Vacuum Science and Technology B*, Vol. 17, No. 2, pp. 705-709.

[73] Choi, W. B., Cuomo, J. J., Zhirnov, V. V., Myers, A. F., Hren, J. J., "Field Emission From Silicon and Molybdenum Tips Coated With Diamond Powder by Dielectrophoresis,"

Applied Physics Letters, Vol. 68, No. 5, 1996, pp. 720-722.

[74] Liu J., Zhirnov, V. V., Wojak, G. J., Myers, A. F., Choi, W. B., Hren, J. J., Wolter, S. D., McClure, M. T., Stoner, B. R., Glass, J. T., "Electron Emission From Diamond Coated Silicon Field Emitters," *Applied Physics Letters*, Vol. 65, No. 22, 1994, pp. 2842-2844.

[75] Liu, J., Zhirnov, V. V., Myers, A. F., Wojak, G. J., Choi, W. B., Hren, J. J., Wolter, S. D., McClure, M. T., Stoner, B. R., Glass, J. T., "Field Emission Characteristics of Diamond Coated Silicon Field Emitters," *Journal of Vacuum Science and Technology B*, Vol. 13, No. 2, 1995, pp. 422-426.

[76] Albin, S., Fu, W. Varghese, A., Lavarias, A. C., Myneni, G. R., "Diamond Coated Silicon Field Emitter Array," *Journal of Vacuum Science and Technology A*, Vol. 17, No. 4, 1999, pp. 2104-2108.

[77] Runyan, W. R., Bean, K. E., Semiconductor Integrated Circuit Processing Technology, Massachusetts: Addison-Wesley Publishing Company, Inc., 1990, pp. 99, 53-112, 161-236, 242-288.

[78] Sze, S. M., VLSI Technology, New York: McGraw-Hill Book Company, Inc.,1988, pp. 98-137, 141-180.

[79] Bean, Kenneth E., "Anisotropic Etching of Silicon," *IEEE Transactions on Electron Devices*, Vol. ED-25, No. 10, 1978, pp. 1185-1193.

[80] Landsberger, L. M., Naseh, S., Kahrizi, M., Paranjape, M., "On Hillocks Generated During Anisotropic Etching of Si in TMAH," *Journal of Microelectromechanical Systems*, Vol. 5, No. 2, 1996, 106-116.

[81] Tabata, O., Asahi, R., Funabashi, H., Shimaoka, K., Sugiyama, S., "Anisotropic Etching of Silicon in TMAH Solutions," *Sensors and Actuators A*, Vol. 34, 1992, pp. 51-57.

[82] Ristic, Lj., Hughes, H., Shemansky, F., "Bulk Micromachining Technology," in Sensor Technology and Devices, Ristic, Lj., ed., Massachusetts: Artech House, 1994, pp. 63-66.

[83] Naseh, S., Landsberger, L. M., Paranjape, M., Kahrizi, M., "Experimental Investigations of Anisotropic Etching of Si in Tetramethyl Ammonium Hydroxide," *Canadian Journal of Physics (Supplemental)*, Vol. 74, 1996, pp. S79-S84.

[84] Tabata, O., "pH-Controlled TMAH Etchants for Silicon Micromachining," *Sensors and Actuators A*, Vol. 53, 1996, pp. 335-339.

[85] Nemirovsky, Y., El-Bahar, A., "The Non Equilibrium Band Model of Silicon in TMAH and in Anisotropic Electrochemical Alkaline Etching Solutions," *Sensors and Actuators A*,

Vol. 75, 1999, pp. 205-214.

[86] Merlos, A., Acero, M., Bao, M. H., Bausells, J., Esteve, J., "TMAH/IPA Anisotropic Etching Characteristics," *Sensors and Actuators A*, Vol. 37-38, 1993, pp. 737-743.

[87] Huq, S. E., Grayer, G. H., Moon, S. W., Prewett, P. D., "Fabrication and Characterisation of Ultra Sharp Silicon Field Emitters," *Materials Science & Engineering B*, Vol. B51, 1998, pp. 150-153.

[88] Robertson, J., Gerber, J., Sattel, S., Weiler, M., Jung, K., Ehrhardt, H., "Mechanism of Bias-Enhanced Nucleation of Diamond on Si," *Applied Physics Letters*, Vol. 66, No. 24, 1995, pp. 3287-3289.

[89] Stoner, B. R., Ma, G.-H. M., Wolter, S. D., Glass, J. T., "Characterization of Bias-Enhanced Nucleation of Diamond on Silicon by In Vacuo Surface Analysis and Transmission Electron Microscopy," *Physical Review B*, Vol. 45, No. 19, 1992, pp. 11067-11084.

[90] Weimer, W. A., Cerio, F. M., Johnson, C. E., "Examination of the Chemistry Involved in Microwave Plasma Assisted Chemical Vapor Deposition of Diamond," *Journal of Materials Research*," Vol. 6, No. 10, 1991, pp. 2134-2144.

[91] Nasser, Essam, Fundamentals of Gaseous Ionization and Plasma Electronics, New York: John Wiley & Sons, Inc., 1971, pp. 13-17.

[92] Glang, R., "Vacuum Evaporation," in Handbook of Thin Film Technology, Maissel, L. I., ed., Glang, R., ed., New York: McGraw-Hill, 1970, p. 1-24.

[93] Sugino, T., Kuriyama, K., Kimura, C., Kawasaki, S., "Temperature Dependence of Field Emission Characteristics of Phosphorus-Doped Polycrystalline Diamond Films," *Applied Physics Letters*, Vol. 73, No. 2, 1998, pp. 268-270.

[94] Glesener, J. W., Morrish, A. A., "Investigation of the Temperature Dependence of the Field Emission Current of Polycrystalline Diamond Films," *Applied Physics Letters*, Vol. 69, No. 6, 1996, pp. 785-787.

[95] Wallis, G., Pomerantz, D. I., "Field Assisted Glass-Metal Sealing," *Journal of Applied Physics*, Vol. 40, No. 10, 1969, pp. 3946-3949.

[96] Anthony, T. R., "Anodic Bonding of Imperfect Surfaces," *Journal of Applied Physics*, Vol. 54, No. 5, 1983, pp. 2419-2428.

[97] Choi, W. B., Ju, B. K., Lee, Y. H., Haskard, M. R., Sung, M. Y., Oh, M. H., "Anodic Bonding Technique Under Low Temperature and Low Voltage Using Evaporated Glass,"

Journal of Vacuum Science and Technology B, Vol. 15, No. 2, 1997, pp. 477-481.

[98] Anthony, T. R., "Dielectric Isolation of Silicon by Anodic Bonding," *Journal of Applied Physics*, Vol. 58, No. 3, 1985, pp.1240-1247.

[99] Shimbo, M., Furukawa, K., Fukuda, K., Tanzawa, K., "Silicon-to-Silicon Direct Bonding Method," *Journal of Applied Physics*, Vol. 60, No. 8, 1986, pp. 2987-2989.

[100] Enisherlova, K. L., Rusak, T. F., Chervyakova, E. N., Vinogradov, R. N., "SOI-Structures Produced by the Silicon Direct Bonding Method," *Material Science and Engineering B*, Vol. B46, 1997, pp. 33-37.

[101] Kissinger, G., Kissinger, W., "Hydrophilicity of Silicon Wafers for Direct Bonding," *Physica Status Solidi A*, Vol. 123, No. 85, 1991, pp. 185-192.

[102] Tong, Q. Y., Gosele, U., "Thickness Considerations in Direct Silicon Wafer Bonding," *Journal of the Electrochemical Society*, Vol. 142, No. 11, 1995, pp. 3975-3979.

[103] Kim, E. D., Kim, N. K., Kim, S. C., Grekhov, I. V., Argunova, T. V., Kostina, L. S., Kudryavtseva, T. V., "Silicon Direct Bonding Technology Employing a Regularly Grooved Surface," *Electronics Letters*, Vol. 31, No. 23, 1995, pp. 2047-2048.

[104] Ljungberg, K. Soderbarg, A., Bengtsson, S. Jauhiainen, A., "Characterization of Spontaneously Bonded Hydrophobic Silicon Surfaces," *Journal of the Electrochemical Society*, Vol. 141, No. 2, 1994, pp. 562-566.

[105] Farrens, S. N., Hunt, C. E., Roberds, B. E., Smith, J. K., "A Kinetics Study of the Bond Strength of Direct Bonded Wafers," *Journal of the Electrochemical Society*, Vol. 141, No. 11, 1994, pp. 3225-3230.

[106] Wiget, R., Peczs, B., Burte, E. P., "Silicon Direct Bonding (SDB) - A Substrate Material For Electronic Devices," *International Journal of Electronics*, Vol. 81, No. 6, 1996, pp. 629-642.

[107] Bengtsson, S., Engstrom, O., "Low-Temperature Preparation of Silicon/Silicon Interfaces by the Silicon-to-Silicon Direct Bonding Method," *Journal of the Electrochemical Society*, Vol. 137, No. 7, 1990, pp. 2297-2303.

[108] Jiao, J., Lu, D., Xiong, B., Wang, W., "Low-Temperature Silicon Direct Bonding and Interface Behaviours," *Sensors and Actuators A*, Vol. 50, 1995, pp. 117-120.

[109] Harendt, C., Hunt, C. E., Appel, W., Graf, H. G., Hofflinger, B., Penteker, E., "Silicon on Insulator Material by Wafer Bonding," *Journal of Electronic Materials*, Vol. 20, No. 3, 1991, pp. 267-27.